Development/Plasticity/Repair

Ca$_v$1.3 Calcium Channels Are Required for Normal Development of the Auditory Brainstem

Jan J. Hirtz,[1] **Michael Boesen,**[1] **Nadine Braun,**[1] **Joachim W. Deitmer,**[2] **Florian Kramer,**[1] **Christian Lohr,**[2] **Britta Müller,**[1] **Hans Gerd Nothwang,**[1,3] **Jörg Striessnig,**[4] **Stefan Löhrke,**[1] **and Eckhard Friauf**[1]

[1]Animal Physiology Group and [2]General Zoology, Department of Biology, University of Kaiserslautern, D-67653 Kaiserslautern, Germany, [3]Department of Neurogenetics, Institute for Biology and Environmental Sciences, University of Oldenburg, D-26129 Oldenburg, Germany, and [4]Institute of Pharmacy, Pharmacology and Toxicology, Center of Molecular Biosciences, University of Innsbruck, A-6020 Innsbruck, Austria

Within the Ca$_v$1 family of voltage-gated calcium channels, Ca$_v$1.2 and Ca$_v$1.3 channels are the predominant subtypes in the brain. Whereas specific functions for each subtype were described in the adult brain, their role in brain development is poorly understood. Here we assess the role of Ca$_v$1.3 subunits in the activity-dependent development of the auditory brainstem. We used Ca$_v$1.3-deficient (Ca$_v$1.3$^{-/-}$) mice because these mice lack cochlea-driven activity that deprives the auditory centers from peripheral input. We found a drastically reduced volume in all auditory brainstem centers (range 25–59%, total 35%), which was manifest before hearing onset. A reduction was not obvious outside the auditory system. The lateral superior olive (LSO) was strikingly malformed in Ca$_v$1.3$^{-/-}$ mice and had fewer neurons (1/3 less). The remaining LSO neurons displayed normal dendritic trees and received functional glutamatergic input, yet they fired action potentials predominantly with a multiple pattern upon depolarization, in contrast to the single firing pattern prevalent in controls. The latter finding appears to be due to a reduction of dendrototoxin-sensitive potassium conductances, presumably mediated through the K$_v$1.2 subtype. Fura2 imaging provided evidence for functional Ca$_v$1.3 channels in the LSO of wild-type mice. Our results imply that Ca$_v$1.3 channels are indispensable for the development of the central auditory system. We propose that the unique LSO phenotype in Ca$_v$1.3$^{-/-}$ mice, which hitherto was not described in other hereditary deafness models, is caused by the synergistic contribution of two factors: on-site loss of Ca$_v$1.3 channels in the neurons plus lack of peripheral input.

Introduction

Neurons express multiple types of voltage-gated calcium channels (VGCCs), each with specific electrophysiological properties and functional roles. Ten genes encode the pore-forming α1 subunits, whose homologies divide the VGCCs into three families (Ca$_v$1.1–1.4, Ca$_v$2.1–2.3, Ca$_v$3.1–3.3) (Catterall et al., 2005).

Within the Ca$_v$1 calcium channel family (alias L-type Ca^{2+} channels), Ca$_v$1.2 and Ca$_v$1.3 channels are the predominant isoforms in the brain (Sinnegger-Brauns et al., 2009), where they display an overlapping expression pattern. Although a presynaptic location cannot be excluded (Tippens et al., 2008; Leitch et al., 2009), they have been localized predominantly to the somatic and dendritic compartments (Hell et al., 1993; Lima and Marrion, 2007; Suki-asyan et al., 2009). Here, they mediate persistent Ca^{2+} influx, sustain plateau potentials, and support pacemaking (Puopolo et al., 2007; Guzman et al., 2009). They also amplify input signals and activate biochemical pathways that involve changes in gene expression and ultimately lead to long-term alterations in neuronal function (for review, see Weick et al., 2005).

In the peripheral auditory system, Ca$_v$1.3 channels govern vesicle fusion and subsequent neurotransmitter release from cochlear inner hair cells (IHCs) onto afferent auditory nerve fibers (Platzer et al., 2000; Brandt et al., 2003). Cochlear hair cells of Ca$_v$1.3 subunit-deficient (Ca$_v$1.3$^{-/-}$) mice display a complex developmental failure and degenerate after postnatal day (P) 15 (Beutner and Moser, 2001; Michna et al., 2003; Glueckert et al., 2003; Nemzou et al., 2006), emphasizing the crucial importance of this channel isoform for normal hair cell development. Ca$_v$1.3 channels are functional in the IHCs already in neonatal mice, thus long before hearing onset and at times when spontaneous activity in the cochlea (Kros et al., 1998; Beutner and Moser, 2001) drives the synaptic activity in the subsequent auditory pathway (Tritsch et al., 2010). Spontaneous neuronal activity

patterns appear to be a prerequisite for neuron survival and the generation of orderly connections in the auditory (Friauf and Lohmann, 1999; Kandler and Gillespie, 2005; Kandler et al., 2009) and other systems [e.g., visual: Cang et al. (2005), Huberman et al. (2008); somatosensory: Khazipov et al. (2004); hippocampus: Khazipov et al. (2001); cerebral cortex: Khazipov and Luhmann (2006)]. The nature and functional role of these early activity patterns are therefore of central interest in neuroscience. To address the role of L-type VGCCs in circuit formation and to specifically tackle Ca$_v$1.3 channels, we here used Ca$_v$1.3$^{-/-}$ mice and analyzed the development of their auditory brainstem centers morphologically and physiologically. Emphasis was laid on the lateral superior olive (LSO), a small, yet conspicuous relay center in the medullary brainstem that holds a key position in the sound localization process (Caird and Klinke, 1983; Sanes, 1990; Grothe et al., 2010). Our data demonstrate developmental aberrances in the Ca$_v$1.3$^{-/-}$ brainstem in general, yet to a disproportionately high degree in the auditory relay centers. The most striking malformation occurred in the Ca$_v$1.3$^{-/-}$ LSO, which lost its characteristic U shape and ∼1/3 of its neurons. As this phenotype differs from that seen in other hereditary deafness models (Webster, 1985; Youssoufian et al., 2008), our results imply that both peripheral and central sources contribute to the defects, consistent with the observation that functional Ca$_v$1.3 channels are present in LSO neurons.

Materials and Methods

Animals. Experiments were performed on wild-type (WT) mice and Ca$_v$1.3$^{-/-}$ mice that lack the Ca$_v$1.3 α_1 subunit of L-type VGCCs (Platzer et al., 2000). Both genotypes were bred on a C57BL/6N background and animals of both genders were used. Their treatment was in accordance with the German law for conducting animal experiments and followed the NIH guide for the care and use of laboratory animals.

Immunohistochemistry. Deeply anesthetized mice (700 mg chloral hydrate per kg body weight, i.p.) were transcardially perfused with 15 mM PBS (pH 7.4), followed by Zamboni's solution (2% paraformaldehyde, 15% picric acid in 150 mM phosphate buffer). Brains were postfixed in Zamboni's solution overnight and then incubated in 30% sucrose/PBS for cryoprotection for at least 24 h. Thereafter, 30-μm-thick coronal sections were cut through the brainstem with an HM 400R sliding microtome (Microm), collected in 15% sucrose/PBS, rinsed in PBS, and blocked for 1 h in 3% bovine serum albumin, 10% goat serum, and 0.3% Triton X-100 in TRIS-buffered saline, pH 7.4. The rabbit-anti-VGLUT1 antibody, a generous gift by Dr. S. El Mestikawy (Inserm U513, Créteil Cedex, France), was diluted 1:1000. The mouse-anti-calbindin-D$_{28k}$ antibody (Sigma-Aldrich) was diluted 1:5000. The mouse-anti-Kv1.1 and mouse-anti-Kv1.2 antibodies (NeuroMab, UC Davis/NIH NeuroMab Facility, Davis, CA) were diluted 1:500. Antisera were added to the blocking solution and sections were incubated for 20 h at 8°C. After three rinses in PBS, sections were transferred into TRIS-buffered saline with 0.3% Triton X-100, 1% bovine serum albumin, and 1% goat serum. In here, they were incubated for 1.5 h at room temperature with the secondary antibodies, goat-anti-rabbit or goat-anti-mouse, both conjugated to Alexa Fluor 488 and diluted 1:1000 (Invitrogen). After four rinsing steps, the sections were mounted and air dried. Home-made mounting medium that included anti-fading substances was used to cover the sections. Images were taken on an LSM 510 confocal microscope (Zeiss) equipped with an argon laser (488 nm) and appropriate excitation and emission filters (488 nm excitation, filter BP 505–550). A Plan-Neofluar 10×/0.3 objective (Zeiss) was used, and pinhole settings were chosen to achieve optical sections of <12 μm thickness. Images were further processed with Zeiss LSM Image browser software 2.80 (Zeiss) and ImageJ 1.34 s (NIH). K$_v$1.1 and K$_v$1.2 immunoreactivity was visualized by DAB labeling as described earlier (Friauf et al., 1999). Photomicrographs of DAB-labeled specimens were obtained with an Axioskop 2 microscope (Zeiss) equipped with a CCD camera (DP-20, Olympus).

Table 1. Composition of solutions used for patch-clamp recordings and Ca^{2+} imaging

Preparation solution	NaHCO$_3$, 25; NaH$_2$PO$_4$, 1.25; KCl, 2.5; MgCl$_2$, 1; CaCl$_2$, 2; D- glucose, 260; sodium pyruvate, 2; myo-inositol, 3; kynurenic acid, 1
ACSF	NaCl, 125; NaHCO$_3$, 25; NaH$_2$PO$_4$, 1.25; KCl, 2.5; MgCl$_2$, 1; CaCl$_2$, 2; D- glucose, 10; sodium pyruvate, 2; myo-inositol, 3; ascorbic acid, 0.4
Intracellular solution	Potassium gluconate, 135; EGTA, 1; MgCl$_2$, 2; HEPES, 10; CaCl$_2$, 0.1; Na$_2$ATP, 2; Na$_2$GTP, 0.3; pH 7.3 with KOH
Cesium-based intracellular solution	CsCl, 125; TEA-Cl, 10, EGTA, 1; MgCl$_2$, 2; HEPES, 10; CaCl$_2$, 0.1; Na$_2$ATP, 2; Na$_2$GTP, 0.3; pH 7.3 with CsOH

Concentrations are given in mM. Preparation solution and ACSF were at pH 7.4 when bubbled with 95% O$_2$ and 5% CO$_2$.

Nissl staining. Coronal sections of the brainstem were obtained from perfusion-fixed brains (4% paraformaldehyde in 150 mM phosphate buffer) or from unfixed brains that had been rapidly frozen in liquid isopentan (AppliChem) immediately after decapitation. Thirty-micrometer-thick sections were cut on a sliding microtome or a CM3000 cryostat (Leica). Slide-mounted sections were defatted overnight in a chloroform/ethanol solution (1:2) followed by 100% ethanol for 1 h. Hydration was performed in a descending ethanol series, ending in Aqua dest. After Nissl staining for 1 min in thionin solution, sections were dehydrated in an ascending ethanol series and xylene before coverslips were mounted with entellan (Merck). Photomicrographs of Nissl-stained sections were obtained with an Axioskop 2 microscope (Zeiss) equipped with a CCD camera (F-View or DP-20, Olympus), using cell-F 3.0 (Olympus) and ImageJ for analysis. The volumes of the brainstem, of the nuclei of the lateral lemniscus, and of the inferior colliculus were determined from section overviews obtained with a Nikon Super Coolscan 9000 slide scanner. The brainstem was defined as the region between the caudally located nucleus ambiguus and the rostrally located Nucleus ruber, excluding the cerebellum. Volumes were calculated by multiplying the outlined area with the thickness of each section (30 μm). Images of whole perfusion-fixed brains were obtained using a stereoscope (SZX7, Olympus with DP-20 CCD camera), and ImageJ was used for analysis.

Electrophysiology. Patch-clamp recordings in the whole-cell configuration were performed at room temperature on LSO neurons in acutely isolated brainstem slices. Animals at P3 ± 1, P12 ± 1, and P19 ± 1 (taking the day of birth as P0) were decapitated and their brains were quickly removed. Coronal brainstem slices containing the superior olivary complex (SOC) (270–300 μm thick, 1–2 slices per animal) were vibrocut (VT1000 or VT1200 S, Leica) in ice-cold solution (for composition, see Table 1) and stored at 37°C for 1 h in artificial CSF (ACSF) (Table 1). Thereafter, they were stored at room temperature before being transferred into a recording chamber in which they were continually superfused with ACSF. The chamber was mounted on an upright microscope (Eclipse E600FN, Nikon) equipped with differential interference contrast optics (Nikon objectives: 4t CFI Achromat, 0.1 NA; 60× CFI Fluor W, 1.0 NA) and an infrared video camera system (CCD camera C5405–01, Hamamatsu; or CCD camera VX45, PCO computer optics; PC frame grabber card, pciGrabber-4plus, PHYTEK).

Patch pipettes were pulled from borosilicate glass capillaries (GB150(F)-8P, Science Products) with a horizontal puller (P-87, Sutter Instruments). They had resistances of 3–6 MΩ when filled with intracellular solution (Table 1) (liquid junction potential 16.7 mV) and were connected to an Axopatch-1D patch-clamp amplifier (Molecular Devices) or an EPC 10 patch-clamp amplifier (HEKA Elektronik). For recordings of NMDA receptor-mediated EPSCs (NMDA EPSCs), patch pipettes were filled with a cesium-based solution (Table 1) (liquid junction potential 4.8 mV). The liquid junction potentials were corrected online (recordings with EPC 10) or offline (recordings with Axopatch-1D). Sample frequency was 10–20 kHz and cutoff frequency of low-pass filtering was 8.3–10 kHz. Series resistance was routinely compensated by 50–90%.

To analyze passive membrane properties and spiking characteristics, recordings were performed in the current-clamp mode, and 200-ms-

long rectangular current pulses were injected from −200 pA to 450 pA in 50 pA steps. Input resistance was determined as the slope of the current–voltage relationships between −50 and 0 pA. To isolate potassium currents from voltage-activated sodium and calcium currents, experiments were performed in the presence of 0.5 μM TTX (Ascent Scientific) and 50 μM CdCl$_2$ (Fluka). To distinguish between low- and high-threshold potassium currents, 100 nM α dendrototoxin (α-DTX, Sigma-Aldrich) or 1 mM tetraethylammonium (TEA, AppliChem) were applied. To selectively block K$_V$1.1-mediated currents, DTX-K was applied (Sigma-Aldrich, 100 nM). Voltage step protocols (10 mV steps from −70 to +20 mV, each lasting 400 ms) were used, and the α-DTX, DTX-K, or TEA-sensitive currents were obtained by subtracting the current responses in the presence of the drug from those in control solution. Recordings were obtained with an Axopatch-1D and analyzed with ClampFit 8.2.0.235.

To evoke EPSCs, a theta glass electrode (TST150–6, WPI) with a diameter of 10–20 μm was filled with extracellular solution and placed lateral to the LSO. Electrical stimuli consisted of 100-μs-long monopolar pulses shaped with a pulse generator (Master 8, A.M.P.I.) and applied through a stimulus isolator unit (A360, WPI). The current amplitude of the stimuli was set to twofold threshold to achieve stable synaptic responses. Inhibitory currents mediated via glycine and GABA$_A$ receptors were routinely blocked by application of 2 μM strychnine (Fluka) and 10 μM SR95531 (Sigma-Aldrich or Ascent Scientific). To distinguish between nonNMDA EPSCs and NMDA EPSCs, the holding potential (V_H) was set to −70 mV and +40 mV, respectively (see legend to Fig. 11 for further details). Averages of 40 single traces were generated for further analysis. Recordings were obtained with an EPC10 and analyzed with FitMaster 2.20 (HEKA Elektronik) and MiniAnalysis 6.0.3 (Synaptosoft).

Electroporation and analysis of soma-dendritic morphology. Patch pipettes were filled with slightly modified intracellular solution containing 1 mM Alexa 568-conjugated hydrazine salt (3 kDa, Invitrogen). Electroporation and dye injection of visually identified LSO neurons in acutely prepared slices (see above for details) was done as follows: at ∼1 μm distance from the soma of LSO cells, one to five voltage pulses (20 V amplitude, 25 ms duration) were applied using the pulse generator and isolator (Iso-Flex, A.M.P.I.). Slices were fixed overnight in 4% PFA, rinsed three times in PBS and mounted. Optic stacks of filled neurons were created with an LSM 510 confocal microscope (Zeiss), equipped with a helium neon laser (568 nm) and an EC Plan-Neofluar 40×/1.30 Oil DIC M27 objective (Zeiss). Images were subsequently analyzed with LSM Image Browser 4.2 (Zeiss). The freeware Neuromantic was used for reconstructions (www.reading.ac.uk/neuromantic). Neurons were classified into one of three groups: multipolar if primary dendrites arose from all sides of the soma, bipolar if primary dendrites arose from two opposite poles, and unipolar if primary dendrites emerged from only one pole. Sholl analysis was performed on whole stack projections. To do so, a ring was drawn around the cell soma, followed by concentric rings, each adding 10 μm to the radius. For each ring, all dendritic intersections were counted.

Ca^{2+} imaging. Coronal slices of 250 μm thickness were cut as described above. After incubation at 37°C for 1 h, slices were stained in ACSF containing 4 μM Fura2-AM (Invitrogen) and 0.01% pluronic acid (Invitrogen) for 1 h in darkness. Imaging experiments were performed using an upright EX 50 WI Olympus microscope equipped with a 5× and 40× LUMPlanFI objective (Olympus), using excitation wavelengths of 340 and 380 nm, the excitation maximum for Ca^{2+}-bound and unbound Fura2, respectively. Emissions fluorescence was measured with a CCD camera (U-TV0.5XC, Olympus) at a wavelength of 510 nm. Single somata of LSO neurons were selected as regions of interest and the ratio of the emissions (F_{340}/F_{380}) was calculated. Slices were continually perfused with ACSF. To depolarize cells, 30 mM K$^+$ was applied in substitute for Na$^+$. To block L-type Ca^{2+} channels, 20 μM nifedipine (Sigma-Aldrich) was added to the ACSF. At the end of each experiment, a 0 K$^+$ solution (substituted by Na$^+$) was applied. As only glia cells, but not neurons, react with a Ca^{2+} influx in 0 K$^+$ (Dallwig et al., 2000), recordings from such cells were excluded from further analysis. Setup control and analysis were performed with TILLvisION v4.01 (Till Photonics GmbH).

Statistics. To assess for statistical significance (Winstat, R. Fitch Software), all data sets were checked for Gaussian distribution, and outliers
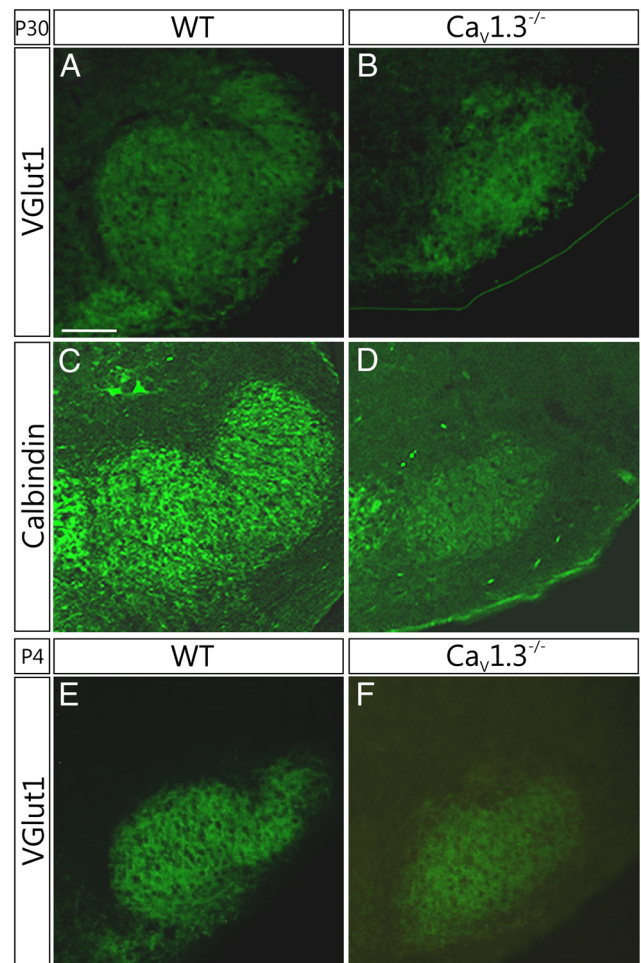

Figure 1. Malformed LSO in Ca$_v$1.3 $^{-/-}$ mice. **A, B**, Immunofluorescence of VGluT1 in coronal brainstem sections of a P30 WT mouse, revealing the typical U shape of the mouse LSO. Remarkably, this U shape was not present in age-matched Ca$_v$1.3 $^{-/-}$ mice. **C, D**, The malformation of the LSO at P30 was confirmed by calbindin-D$_{28k}$ immunoreactivity. **E, F**, Morphological differences were already present at P4 as demonstrated by VGluT1 immunoreactivity. Scale bar: (in **A**) **A–F**, 200 μm. Dorsal is up, lateral is to the right.

(more than four times SD above/below the mean) were excluded. Unless noted otherwise, an unpaired, two-tailed Student's t test was performed. In case of a non-Gaussian distribution, a U test was performed with same significance values as in the t test. Error bars in the diagrams illustrate the SEM. In some diagrams (see Fig. 2 E–G), dot plots of single values were added to the bars to illustrate their distribution.

Results

Malformed LSO in Ca$_v$1.3 $^{-/-}$ mice

Ca$_v$1.3 $^{-/-}$ mice are congenitally deaf because the lack of the pore-forming α_{1D} subunit results in an absence of calcium-induced glutamate exocytosis from the IHCs (Platzer et al., 2000). This leads to the lack of cochlea-driven activity in the auditory nerve fibers and deprives the auditory brainstem nuclei of their peripheral input. Because maturation of auditory microcircuits is an activity-dependent process, we reasoned that Ca$_v$1.3 $^{-/-}$ mice might display an impaired development of auditory brainstem structures. In an initial screening experiment, we therefore used immunofluorescent histochemistry with antisera to the vesicular glutamate transporter VGlut1, a presynaptic marker for excitatory glutamatergic inputs, in the auditory brainstem of young adult (P30) mice (Blaesse et al., 2005). Astonishingly, the LSO of Ca$_v$1.3 $^{-/-}$ mice showed a strikingly altered
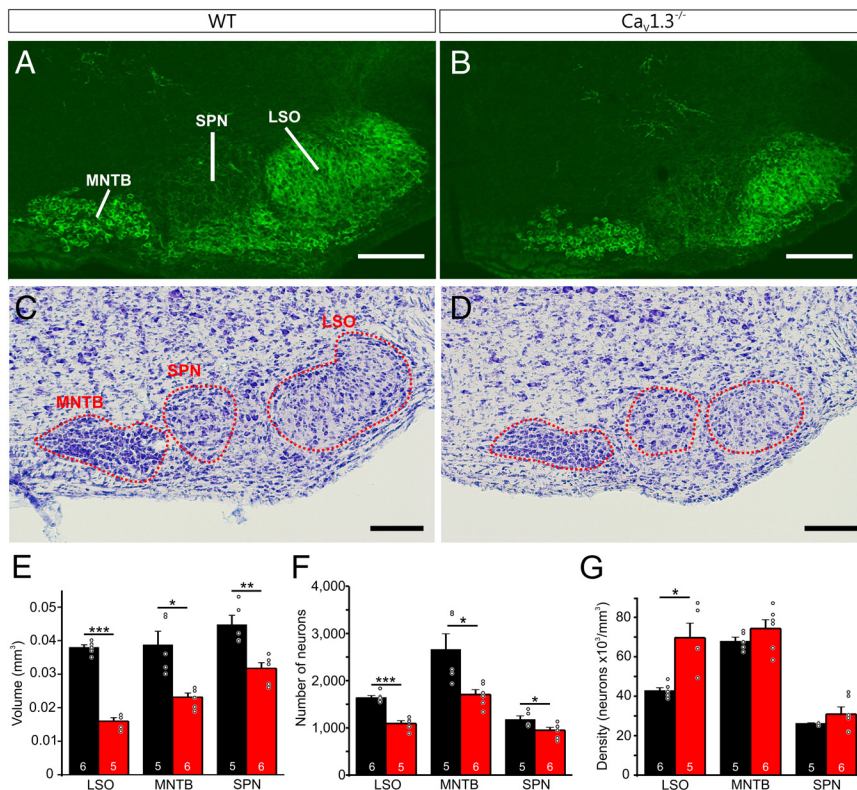
Figure 2. Drastic volume decrease in SOC nuclei of Ca$_v$1.3$^{-/-}$ mice. ***A***, ***B***, VGluT1 in the SOC of P12 WT and Ca$_v$1.3$^{-/-}$ mice. MNTB, SPN, and LSO appear to be decreased in volume. ***C***, ***D***, Nissl-staining of the SOC at P12 was used for volume quantification. ***E***, The volume of MNTB, SPN, and LSO was lower in Ca$_v$1.3$^{-/-}$ mice compared with WT mice. ***F***, Ca$_v$1.3$^{-/-}$ mice displayed a lower number of neurons in LSO, MNTB, and SPN. ***G***, Based on the number of neurons and the volume of the nuclei, the density of neurons was found to be higher in the LSO of Ca$_v$1.3$^{-/-}$ mice, with no differences in MNTB and SPN. Scale bars: ***A–D***, 200 μm. Dorsal is up, lateral is to the right. Black bars and red bars in ***E–G*** represent data from WT and Ca$_v$1.3$^{-/-}$ mice, respectively. Numbers in bars depict number of analyzed nuclei, three animals for each genotype. Color coding (black: WT; red: Ca$_v$1.3$^{-/-}$) also applies to subsequent figures. Circles in bars depict single values. *$p < 0.05$; **$p < 0.01$; ***$p < 0.001$.

Reduced volume and neuron number of SOC nuclei in Ca$_v$1.3$^{-/-}$ mice

In contrast to the LSO, the other auditory brainstem nuclei, from the level of the cochlear nuclear complex (CN) to the inferior colliculus (IC), did not display striking changes in shape that could be easily discerned at a first glance (Figs. 2 *A–D*, 3, 4). However, the medial nucleus of the trapezoid body (MNTB) and the superior paraolivary nucleus (SPN) appeared to be reduced in size as well (Fig. 2 *A*,*B*). To objectify this impression, we determined the volume of the LSO, MNTB, and SPN (from the individual areas in all coronal sections containing the SOC), determined the number of neurons by counting the number of nucleoli, and calculated the neuron densities from Nissl-stained sections (Fig. 2*C*,*D*). Staining was obtained at P12, because the cytoarchitecture of the auditory brainstem nuclei is well established at this age and because we wanted to age-match with the animals that we analyzed in electrophysiological experiments. The volume of the three SOC nuclei analyzed was significantly lower in Ca$_v$1.3$^{-/-}$ mice than in the WTs (Table 2, Fig. 2*E*). The reduction was most prominent in the LSO (58%), followed by the MNTB and the SPN (41% and 29%, respectively). Ca$_v$1.3$^{-/-}$ mice also displayed a significantly lower neuron number in the LSO (reduced by 33%), the MNTB (35%), and the SPN (19%) (Table 2, Fig. 2*F*). When we finally calculated the neuronal somata density, the LSO displayed a significant increase (62%) in the Ca$_v$1.3$^{-/-}$ animals; no change occurred in the MNTB and the SPN (Table 2, Fig. 2*G*). Together, these data imply structural changes in all SOC nuclei analyzed as a consequence of a loss of functional Ca$_v$1.3 channels, with the LSO being the nucleus that appears to be most heavily affected.

Reduced volume of CN, nuclei of the lateral lemniscus, and IC in Ca$_v$1.3$^{-/-}$ mice

As shown above, the structural alterations in the auditory brainstem of Ca$_v$1.3$^{-/-}$ mice were not limited to the LSO, but present in other SOC nuclei as well. To assess whether they were restricted to the SOC, we next analyzed all auditory brainstem stations in the medulla and the midbrain, namely the CN, the nuclei of the lateral lemniscus (NLL), and the IC. From Nissl-stained coronal sections, we analyzed the cytoarchitecture and determined the volume of auditory brainstem nuclei. In both WT and Ca$_v$1.3$^{-/-}$ animals, the CN could be subdivided into the classic three parts, the dorsal cochlear nucleus (DCN), the posterior ventral cochlear nucleus (PVCN), and the anterior ventral cochlear nucleus (AVCN); the cytoarchitecture in all three parts appeared to be indistinguishable between phenotypes (Fig. 3*A–D*). However, quantification of the nuclear volume (through all sections containing the CN) revealed a significant decrease in all three CN subdivisions of Ca$_v$1.3$^{-/-}$ mice, with the reduction ranging between 37% and 59% (Table 3, Fig. 3*E*). In accordance with the results obtained in the CN, no malformations were ob-

morphology compared with age-matched WT mice (Fig. 1*A*,*B*). Its typical U shape, which is normally present in mice, was not evident, and its size appeared to be reduced in coronal sections.

To confirm that the malformations in the LSO did not merely reflect a changed distribution of VGlut1-positive synaptic terminals, we also applied antisera against other markers. When we immunolabeled the calcium-binding protein calbindin-D$_{28k}$, known to be abundant in the LSO and clearly outlining its shape (Friauf, 1993), we again did not see the U shape and found a decreased size in P30 Ca$_v$1.3$^{-/-}$ animals (Fig. 1*C*,*D*). The same phenotype was obvious with other markers that also clearly reveal the LSO contour, such as the microtubule-associated protein MAP2 and the glycine transporter GlyT2 (data not shown). This demonstrated that the LSO is indeed malformed in young adult Ca$_v$1.3$^{-/-}$ mice.

To pinpoint the time at which the malformation becomes manifested, we extended our immunohistochemistry experiments to P4. We found the same difference as at P30 between phenotypes with VGlut1 (Fig. 1*E*,*F*) and the other markers (data not shown). As hearing onset in mice reportedly occurs between P9 and P14 [C57BL/6J: Shnerson and Willott (1980), Shnerson and Pujol (1982); other strains: Alford and Ruben (1963), Mikaelian and Ruben (1965), Hack (1968), Ehret (1976)], these results thus demonstrated that the malformations are not due to the lack of sound-driven activity, yet occur during prehearing life when auditory circuit formation and consolidation takes place (Boudreau and Tsuchitani, 1970; Kandler et al., 2009).
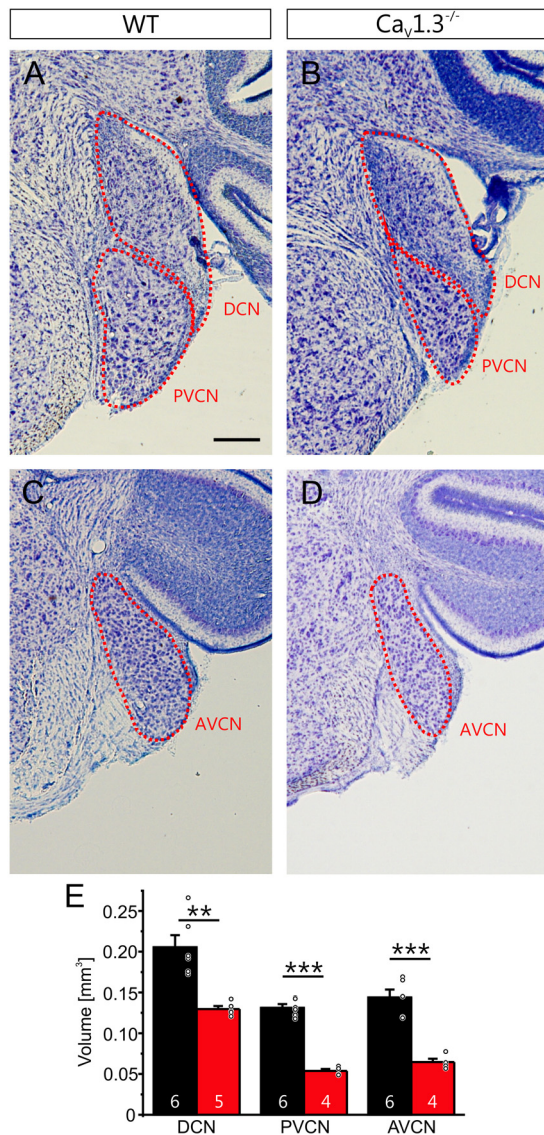
Figure 3. Decreased volume of CN in Ca$_v$1.3$^{-/-}$ mice. ***A–D***, Examples of Nissl-stained sections at P12, containing DCN, PVCN, and AVCN in WT and Ca$_v$1.3$^{-/-}$ mice. ***E***, DCN, PVCN, and AVCN displayed a lower volume in Ca$_v$1.3$^{-/-}$ mice compared with WT mice. Scale bar: (in ***A***) ***A–D***, 200 μm. Dorsal is up, lateral is to the right. Numbers in bars depict number of analyzed nuclei, three animals for each genotype. Circles in bars depict single values. **$p < 0.01$; ***$p < 0.001$.

Figure 4. Decreased volume of NLL and IC in Ca$_v$1.3$^{-/-}$ mice. ***A—D***, Nissl-staining of P12 Ca$_v$1.3$^{-/-}$ and WT mice sections containing the NLL (***A***, ***B***) or the IC (***C***, ***D***). ***E***, Both nuclei showed a decrease in Ca$_v$1.3$^{-/-}$ mice compared with WT mice. Scale bar: (in ***A***) ***A–D***, 500 μm. Dorsal is up, lateral is to the right. Numbers in bars depict number of analyzed nuclei, three animals for each genotype. Circles in bars depict single values. *$p < 0.05$; ***$p < 0.001$.

vious at the gross microscopic level in the NLL and IC of Ca$_v$1.3$^{-/-}$ mice (Fig. 4*A–D*), whereas decreases in volume were observed for both areas (NLL: 25%; IC: 32%) (Table 3, Fig. 4*E*). Together, volume changes were present at all levels of the auditory brainstem in Ca$_v$1.3$^{-/-}$ mice.

Volume reduction in Ca$_v$1.3$^{-/-}$ mice limited to auditory brainstem nuclei
The reduction in volume of the auditory brainstem nuclei that we observed in Ca$_v$1.3$^{-/-}$ animals could be specific and restricted to the auditory system or, alternatively, extend throughout the brainstem or even the whole brain. To address this issue, we measured the surfaces of the neocortex, the tectum, and the cerebellum in whole-brain preparations of perfusion-fixed P12 specimens (Fig. 5*A*). In none of these three regions did we find a difference between WT and Ca$_v$1.3$^{-/-}$ mice (Table 3, Fig. 5*B*),
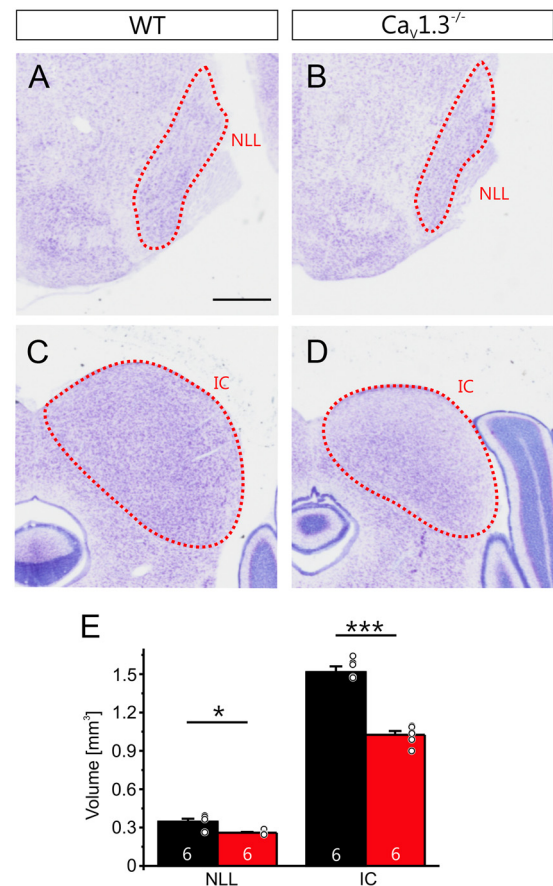
suggesting that the loss of Ca$_v$1.3 does not affect the whole brain per se. To address general brainstem effects, volume values were obtained from Nissl-stained sections. The volume of the brainstem did not differ between the genotypes (Table 3, Fig. 5*C,D*). This indicates a specific susceptibility of the auditory system to Ca$_v$1.3 deficiency. Interestingly, the body weight of Ca$_v$1.3$^{-/-}$ mice is significantly lower than in WT mice (Clark et al., 2003), yet the reduction amounts to only 14% (cf. their Fig. 1*B*), which is considerably less than the volume loss seen throughout the auditory brainstem nuclei (35% in total, ranging from 25% in NLL to 59% in PVCN).

Reduced soma size of SOC and CN neurons in Ca$_v$1.3$^{-/-}$ mice
The volume decrease that we observed in several auditory brainstem nuclei (58% in the LSO) may result from the reduced number of neurons, a smaller soma-dendritic morphology of the neurons, or both. As the loss of 33% of LSO neurons did not strictly correlate with the 58% volume decrease, this implies that an additional factor, besides cell loss, contributes to the malformation and volume decrease. As the size of neuronal somata was shown to correlate positively with the extent and size of their soma-dendritic arbors (Ulfhake and Cullheim, 1981), we determined the soma size by measuring the cross-sectional soma area of Nissl-stained and morphologically categorized neurons (at the level of the nucleolus) in six SOC and CN nuclei (Fig. 6*A*). In the SOC, principal cells of the MNTB and the SPN displayed a sig-

Table 2. Quantification of structural changes in the SOC of Ca$_v$1.3$^{-/-}$ mice

	Volume [mm^3]			Number of neurons			Neuron density [neurons/mm^3]			Cross-sectional soma area [μm^2]		
	WT	Ca$_v$1.3$^{-/-}$	p value/change	WT	Ca$_v$1.3$^{-/-}$	p value/change	WT	Ca$_v$1.3$^{-/-}$	p value/change	WT	Ca$_v$1.3$^{-/-}$	p value/change
LSO	0.038 ± 0.001	0.016 ± 0.001	2.8 × 10^{-8}/ −58%	1,642 ± 45	1,092 ± 60	4 × 10^{-4}/ −33%	42,872 ± 1408	69,455 ± 7006	0.018/+62%	105.6 ± 3.2	98.4 ± 2.4	0.075
MNTB	0.039 ± 0.004	0.023 ± 0.001	0.012/−41%	2,645 ± 329	1,708 ± 101	0.044/−35%	67,865 ± 2032	74,288 ± 4407	0.25	180.1 ± 3.3	169.4 ± 2.9	0.014/−6%
SPN	0.045 ± 0.003	0.032 ± 0.002	0.002/−29%	1,177 ± 74	950 ± 63	0.044/−19%	26,243 ± 302	30,874 ± 3545	0.25	226.2 ± 6.4	203.9 ± 5.7	0.01/−10%

For each genotype, three animals were analyzed with nuclei on both sides ($n = 5–6$). The cross-sectional soma area was determined from 116 –132 cells in 23–25 sections.

Table 3. Quantification of volume or surface in several brain areas

	Volume [mm^3]			Cross-sectional soma area [μm^2]			Surface [mm^2]		
	WT	Ca$_v$1.3$^{-/-}$	p value/change	WT	Ca$_v$1.3$^{-/-}$	p value/change	WT	Ca$_v$1.3$^{-/-}$	p value/change
DCN	0.205 ± 0.015	0.130 ± 0.004	0.003/−37%	273.9 ± 5.7	237.1 ± 5.1	3 × 10^{-5}/−13%			
PVCN	0.131 ± 0.005	0.054 ± 0.003	8.5 × 10^{-7}/−59%	320.7 ± 6.9	276.7 ± 6.4	4 × 10^{-5}/−14%			
AVCN	0.144 ± 0.010	0.065 ± 0.005	1.3 × 10^{-4}/−55%	166.4 ± 4.2	152.6 ± 3.1	0.009/−8%			
NLL	0.347 ± 0.023	0.260 ± 0.006	0.012/−25%						
IC	1.516 ± 0.044	1.026 ± 0.029	3.3 × 10^{-6}/−32%						
Brainstem	29.050 ± 1.459	25.343 ± 1.836	0.15						
Neocortex							47.0 ± 1.4	44.0 ± 0.9	0.18
Tectum							5.6 ± 0.4	4.7 ± 0.3	0.28
Cerebellum							12.8 ± 0.4	11.8 ± 0.3	0.28

For each genotype, three animals were analyzed with nuclei on both sides ($n = 4–6$). The cross-sectional soma area was determined from 99 –146 cells in 13–22 sections. Five to six brains were analyzed for surface and brainstem.
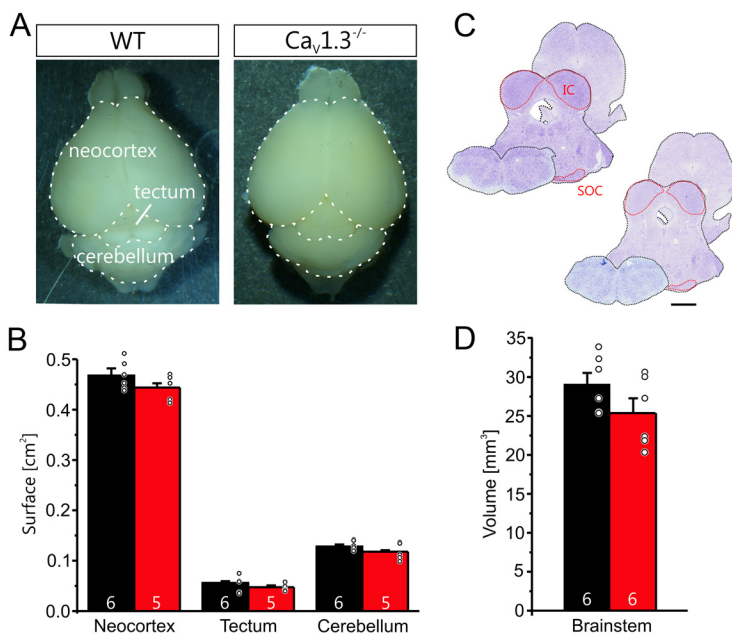

Figure 5. Volume decrease in Ca$_v$1.3$^{-/-}$ mice restricted to the auditory brainstem. **A**, Examples of P12 brains of a Ca$_v$1.3$^{-/-}$ and a WT mouse. Neocortex, tectum, and cerebellum are outlined by dashed lines. **B**, No difference was found between WT and Ca$_v$1.3$^{-/-}$ mice. **C**, Three Nissl-stained coronal sections are shown to illustrate the extent of the brainstem along the caudorostral axis (see Materials and Methods for details); left: P12 WT, right: P12 Ca$_v$1.3$^{-/-}$. **D**, Calculation of brainstem volume as shown in **C** resulted in no difference between the genotypes. Scale bar: (in **C**) **A**, **C**, 1 mm. Numbers in bars depict number of analyzed animals. Circles in bars depict single values.

it loses 1/3 of its neurons, yet the remaining ones display an unchanged soma size.

Minor changes in the soma-dendritic morphology of LSO neurons in Ca$_v$1.3$^{-/-}$ mice

Because the malformation of the LSO in Ca$_v$1.3$^{-/-}$ mice was so striking and more pronounced than in any other auditory nucleus, we focused our further analyses on the LSO and addressed the question of whether the LSO neurons that remain in Ca$_v$1.3$^{-/-}$ mice display normal parameters. In a first step, we analyzed their soma-dendritic morphology. To do so, the fluorescent dye Alexa 568 was injected via electroporation into single LSO neurons in acute P12 ± 1 brainstem slices. Filled LSO neurons could be categorized into multipolar, bipolar, and unipolar neurons both in WT and Ca$_v$1.3$^{-/-}$ mice (Fig. 7A–C), demonstrating that all three neuron types were present despite the loss of Ca$_v$1.3. In fact, the proportion of the three neuron types was unchanged between WT and Ca$_v$1.3$^{-/-}$ mice (Fig. 7H). Likewise, a Sholl analysis of the three cell types revealed no difference between WT and Ca$_v$1.3$^{-/-}$ mice, suggesting a similar complexity of the dendritic trees in the genotypes (Fig. 7D–F). A difference in the extent of the soma-dendritic fields was not found in multipolar neurons between genotypes (Fig. 7G) (WT, 8444 ± 866 μm^2, $n = 24$; Ca$_v$1.3$^{-/-}$, 9225 ± 1004 μm^2, $n = 23$, $p = 0.56$). In contrast, the soma-dendritic field of bipolar neurons differed between genotypes in that it was considerably (81%) larger in Ca$_v$1.3$^{-/-}$ animals (Fig. 7G) (WT, 6690 ± 1168 μm^2, $n = 13$; Ca$_v$1.3$^{-/-}$, 12,074 ± 2011 μm^2, $n = 8$; $p = 0.022$). Together, the soma-dendritic morphology of the LSO neurons that remained

nificantly lower size of their neuronal somata in Ca$_v$1.3$^{-/-}$ mice (6% and 10%, respectively) (Table 2, Fig. 6B). No such effect was seen in spindle-shaped cells in the LSO. In the Ca$_v$1.3$^{-/-}$ CN, giant cells in the DCN, octopus cells in the PVCN, and globular cells in the AVCN all displayed a significantly lower value than in the WT (13%, 14%, and 8%, respectively) (Table 3, Fig. 6C). These results demonstrate that the loss of Ca$_v$1.3 does not only lead to loss of auditory brainstem neurons, but also to shrinkage of those neurons that remain. The LSO forms an exception in that
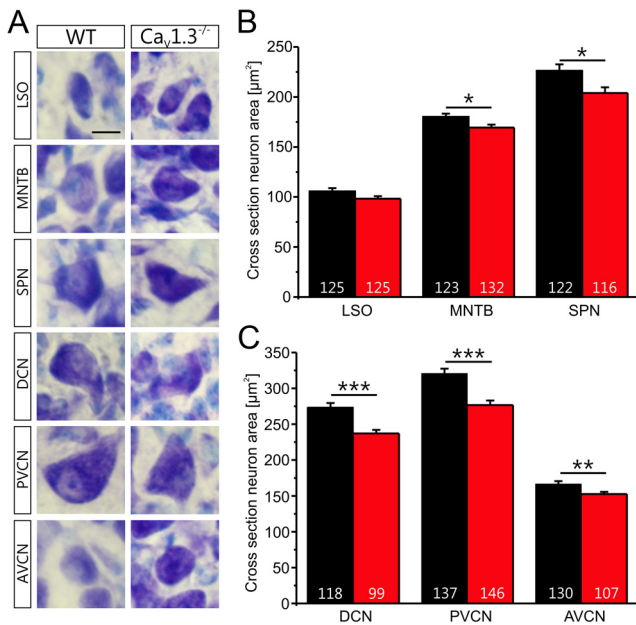
Figure 6. Decrease of neuronal soma size in most parts of the SOC and the CN in Ca$_v$1.3$^{-/-}$ mice. **A**, Examples of 12 Nissl-stained neurons within six nuclei of WT (left column) and Ca$_v$1.3$^{-/-}$ mice (right column) at P12. From top to bottom: LSO (spindle-shaped cells), MNTB (principal cells), SPN (principal cells), DCN (giant cells), PVCN (octopus cells), ACVN (globular cells). **B**, In the SOC, the cross-section neuron area ("neuronal soma size") was lower in Ca$_v$1.3$^{-/-}$ compared with WT mice in the MNTB and the SPN, yet not in the LSO. **C**, The cross section neuron area was also reduced in all three subdivisions of the CN. Scale bar: (all panels in **A**) 5 μm. Numbers in bars depict number of analyzed neurons. Three animals were used for each genotype. *$p < 0.05$; **$p < 0.01$; ***$p < 0.001$.

in Ca$_v$1.3$^{-/-}$ mice differed only slightly from that of WT mice.

Changes in action potential properties and current–voltage responses in Ca$_v$1.3$^{-/-}$ LSO neurons

Whereas the number of LSO neurons was drastically reduced in Ca$_v$1.3$^{-/-}$ mice (Fig. 2F), the soma-dendritic morphology displayed relatively normal properties in the remaining neurons (Fig. 7). To further assess to what extent the remaining LSO neurons were affected, we analyzed their functional characteristics. To do so, we performed patch-clamp recordings in acute slices of P12 ± 1 WT and Ca$_v$1.3$^{-/-}$ mice and determined several passive and active biophysical properties. The resting membrane potential V_{rest} did not differ between genotypes (WT, − 70 ± 0.6 mV, $n = 105$; Ca$_v$1.3$^{-/-}$, − 68.4 ± 0.9 mV; $n = 101$, $p = 0.13$). Injection of depolarizing rectangular current pulses elicited one or multiple action potentials (APs) in both WT and Ca$_v$1.3$^{-/-}$ mice. The kinetics of the first AP differed between genotypes (Fig. 8A,B). APs in Ca$_v$1.3$^{-/-}$ neurons displayed a higher firing threshold (WT, 21 ± 0.7 mV; $n = 103$; Ca$_v$1.3$^{-/-}$, 26.3 ± 0.9 mV; $n = 100$; $p = 3.9E-06$; 25% increase), a higher peak amplitude (WT, 94.3 ± 1.8 mV; $n = 101$; Ca$_v$1.3$^{-/-}$, 103.1 ± 1.5 mV; $n = 99$; $p = 0.0002$; 9% increase), a greater difference between the maximal repolarization and V_{rest} (Δ-to-V_{rest}; WT, 5.2 ± 0.9 mV; $n = 104$; Ca$_v$1.3$^{-/-}$, 10 ± 1.1 mV; $n = 100$; $p = 0.0007$; 92% increase), and a longer half width (WT, 0.86 ± 0.03 ms; $n = 97$; Ca$_v$1.3$^{-/-}$, 1.2 ± 0.05 ms; $n = 98$; $p = 1.5E-08$; 40% increase). We also analyzed the afterhyperpolarization level by measuring the voltage deflection from the 0 mV level (Marcantoni et al., 2010) and found it to be significantly reduced in Ca$_v$1.3$^{-/-}$ mice (WT: −64.7 mV; Ca$_v$1.3$^{-/-}$: −58.2 mV; $p = 0.0002$). Another

difference between the genotypes concerned the number of APs fired during 200-ms-long depolarizing pulses. Whereas 57% (47/82) of the WT neurons responded with a single AP firing pattern and the remaining repetitively with multiple APs, an inverse finding was obtained in Ca$_v$1.3$^{-/-}$ neurons. Here, only 18% (11/62) displayed a single AP firing pattern, while the remaining 82% fired multiple APs (Fig. 8C).

From current injections (amplitudes −50 to −200 pA), we measured the amplitude of voltage changes and found that the response was stronger in Ca$_v$1.3$^{-/-}$ neurons, concerning both the peak amplitude and the steady-state amplitude (data not shown). From the current–voltage relations, we calculated the input resistance and found significantly higher values in Ca$_v$1.3$^{-/-}$ than in WT neurons (386 ± 28 MΩ, $n = 101$ vs 212 ± 25 MΩ, $n = 105$; $p = 4.1E-08$; U test; 82% increase). These results demonstrate the alteration of several biophysical membrane properties of Ca$_v$1.3$^{-/-}$ LSO neurons. Our findings of predominantly multiple AP firing patterns and increased input resistances in Ca$_v$1.3$^{-/-}$ neurons are corroborated by a study in the rat LSO that described two neuronal types: those with multiple AP firing/high input resistance and those with single AP firing/low input resistance (Barnes-Davies et al., 2004).

Altered low-threshold potassium currents in Ca$_v$1.3$^{-/-}$ mice

To a large extent, the AP waveform and the firing behavior of neurons are shaped by voltage-gated potassium currents (Trussell, 1999; Dodson et al., 2002; Rothman and Manis, 2003; Gittelman and Tempel, 2006). To differentiate between various types of currents and to elucidate the molecular basis of our results depicted in Figure 8A–C, we pharmacologically isolated low-threshold (LTK) and high-threshold potassium (HTK) currents in LSO neurons and analyzed their transient and sustained component. In Ca$_v$1.3$^{-/-}$ neurons, α-DTX-sensitive LTK currents were of smaller amplitude than in WT mice for both components. At a membrane potential of 0 mV, the decrease in the transient and the sustained component amounted to 33% and 68%, respectively (Fig. 8D). In contrast, TEA-sensitive HTK currents did not differ between the two groups (Fig. 8E). Our results thus imply that the loss of Ca$_v$1.3 appears to specifically reduce the LTK conductance. Because LTK currents rapidly activate at voltages of ∼20 mV more positive than V_{rest} (Coetzee et al., 1999) and mediate long-lasting potassium ion efflux during an AP (Dodson et al., 2002), our finding of reduced LTK currents can explain the changes in AP kinetics that we found in Ca$_v$1.3$^{-/-}$ LSO neurons, namely the higher peak amplitude, the longer half width, and the higher Δ-to-V_{rest}. Thus, it is likely that the changes in AP kinetics are secondary effects that result from the reduced LTK currents. To confirm that a reduced activity of α-DTX-sensitive channels transforms the firing pattern of LSO neurons from single into multiple, we injected current pulses into WT neurons in the absence and presence of α-DTX. In all LSO neurons ($n = 10$) that displayed a single AP firing pattern in the control situation, the behavior changed into a multiple pattern when 100 nM α-DTX was applied (Fig. 8F), supporting the conclusion that the reduction of LTK conductances is the basis for the observed changes of functional characteristics in Ca$_v$1.3$^{-/-}$ LSO neurons.

α-DTX is most effective toward K$_v$1 channels possessing K$_v$1.1, K$_v$1.2, and K$_v$1.6 subunits (Coetzee et al., 1999; Wang et al., 1999). It exhibits its highest affinity for K$_v$1.2, and only a minor blocking effect is exerted on K$_v$1.3 and K$_v$1.4 channels (Wang et al., 1999). Both K$_v$1.1 and K$_v$1.2 are expressed in the LSO (Grigg et al., 2000; Karcz et al., 2011), in accordance with the fact that
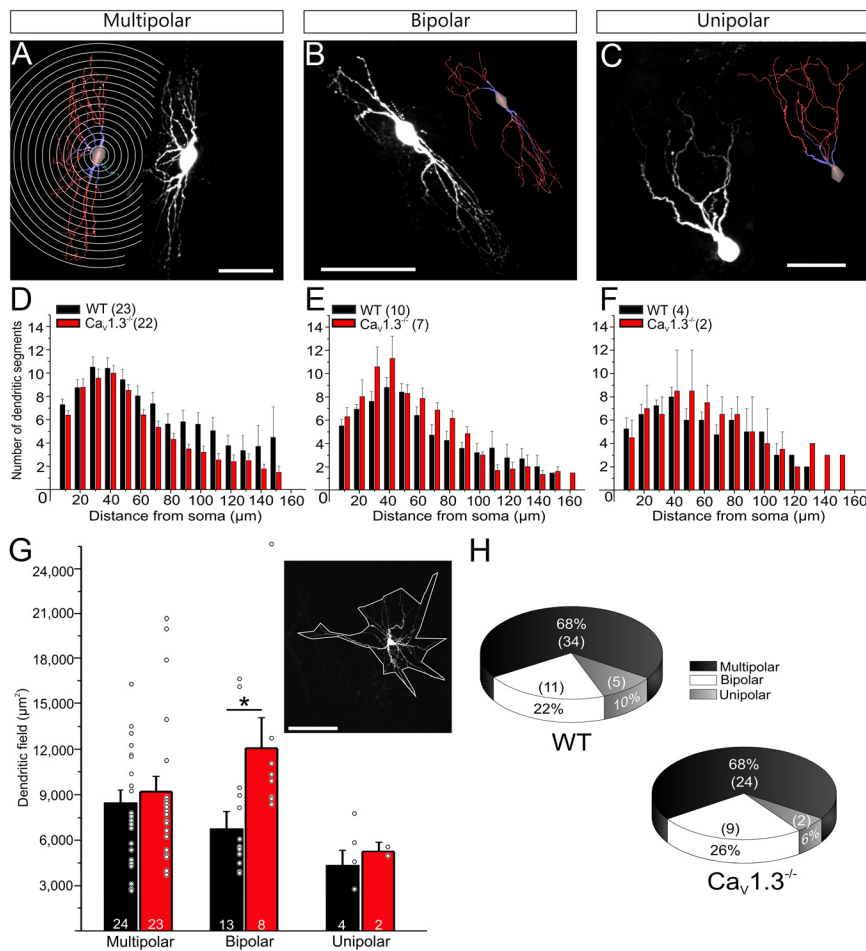
Figure 7. Minor differences in the soma-dendritic morphology of LSO neurons between WT and Ca$_v$1.3$^{-/-}$ mice at P12. **A–C**, Whole stack projections and reconstructions of WT LSO neurons labeled via electroporation of a fluorescent dye. The neurons were categorized into multipolar (**A**), bipolar (**B**), and unipolar (**C**) cells as defined in Materials and Methods. The procedure of the Sholl analysis is exemplarily shown in **A**. Scale bars are 50 μm for the original images. **D–F**, Sholl analysis of multipolar (**D**), bipolar (**E**), and unipolar (**F**) neurons resulted in no differences between genotypes. **G**, The size of the soma-dendritic field of multipolar LSO neurons did not differ between genotypes. In contrast, bipolar LSO neurons of Ca$_v$1.3$^{-/-}$ animals displayed a larger soma-dendritic field than in WT mice. An example of a dendritic field of a multipolar WT neuron is shown in the inset; scale bar, 100 μm. *$p < 0.05$. **H**, The relative amount of the three neuron types in the LSO did not change considerably in Ca$_v$1.3$^{-/-}$ animals. Numbers in bars or brackets depict number of analyzed neurons. Circles in bars depict single values.

these subunits are heavily present in neurons that fire temporally precise action potentials. Moreover, the single firing pattern of MNTB neurons is most likely mediated by heteromers of K$_v$1.1 and K$_v$1.2 (Dodson et al., 2002). These findings prompted us to further distinguish between individual members of the K$_v$1 channel family. To assess whether K$_v$1.1-mediated currents are reduced in LSO neurons of Ca$_v$1.3$^{-/-}$ mice, we applied DTX-K (100 nM), a potent and strictly selective blocker of K$_v$ channels containing the K$_v$1.1 subunit from the venomous mamba snake *Dendroaspis polylepis* (Robertson et al., 1996; Wang et al., 1999). By doing so, we could verify the presence of functional K$_v$1.1 channels in the LSO, but the amount of DTX-K-induced current reduction did not differ between WT and Ca$_v$1.3$^{-/-}$ mice (Fig. 9A), indicating that the K$_v$1.1 subunit is not changed upon the lack of Ca$_v$1.3. Immunohistochemical detection of K$_v$1.1 corroborated this conclusion, as LSO neurons in both genotypes showed a signal of equal strength (Fig. 9B,C). In contrast, K$_v$1.2 immunoreactivity was present in WT mice, yet virtually absent in Ca$_v$1.3$^{-/-}$ mice (Fig. 9D,E), implying that the K$_v$1.2 subunit is reduced upon loss of Ca$_v$1.3 channels and that its reduction is most likely

the cause of most of the above-described alterations associated with potassium conductances.

Normal development of the nonNMDA component of excitatory inputs into the LSO in Ca$_v$1.3$^{-/-}$ mice

In a subsequent series of experiments, we analyzed excitatory synaptic inputs at various ages (P3 ± 1, P12 ± 1, P19 ± 1) to test whether their development was normal in the LSO neurons that remain in Ca$_v$1.3$^{-/-}$ mice. We evoked glutamatergic EPSCs by stimulating the incoming axons in the ventral acoustic stria. The EPSCs were evoked in both phenotypes with similar success rates, showing that functional excitatory synapses are formed in the absence of Ca$_v$1.3. As the neurons were voltage-clamped to −70 mV, NMDA receptors were not activated and, therefore, nonNMDA EPSCs were evoked and analyzed in regard to amplitude, latency, and decay characteristics (Fig. 10). In WT mice, their peak amplitudes increased significantly from P3 to P12, yet not any further between P12 and P19 (Table 4, Fig. 10A,B). This is in line with the increased AMPA-receptor-mediated input seen between P5–P12 in the mouse MNTB (Youssoufian et al., 2005). In LSO neurons of Ca$_v$1.3$^{-/-}$ mice, we observed the same pattern of maturation as in the WT animals; likewise, no difference in peak amplitude was found between genotypes (Table 4, Fig. 10A,B). Paired-pulse protocols were performed to assess possible presynaptic differences (interstimulus intervals 10, 30, 50, 100 ms); again, no difference occurred between the two groups (data not shown). Together, these results show an unimpaired developmental increase of the nonNMDA EPSCs in Ca$_v$1.3$^{-/-}$ LSO neurons.

The onset latency of the nonNMDA EPSCs decreased with age in both WT mice and Ca$_v$1.3$^{-/-}$ mice. Again, no differences were found between the genotypes (Table 4, Fig. 10C,D). The decay time constant τ of the nonNMDA EPSCs displayed no age-dependent change between P3 and P19, neither in WT nor in Ca$_v$1.3$^{-/-}$ mice. As for the amplitude and the latency, no difference was found for τ between the two genotypes, at any given age (Table 4, Fig. 10E,F). Also, no difference was found in the rise time of the EPSCs (data not shown).Together, these results are indicative of an unaffected development of the nonNMDA component in those LSO neurons that remain in Ca$_v$1.3$^{-/-}$ mice, in contrast to previous results in the MNTB that demonstrated a much stronger increase in EPSC amplitude with age in Ca$_v$1.3$^{-/-}$ mice (Erazo-Fischer et al., 2007).

Delayed decline of the NMDA component of excitatory inputs into the LSO in Ca$_v$1.3$^{-/-}$ mice

Like in other brain regions [cortex: Crair and Malenka (1995), Lu et al. (2001); hippocampus: Hsia et al. (1998)], the NMDA com-
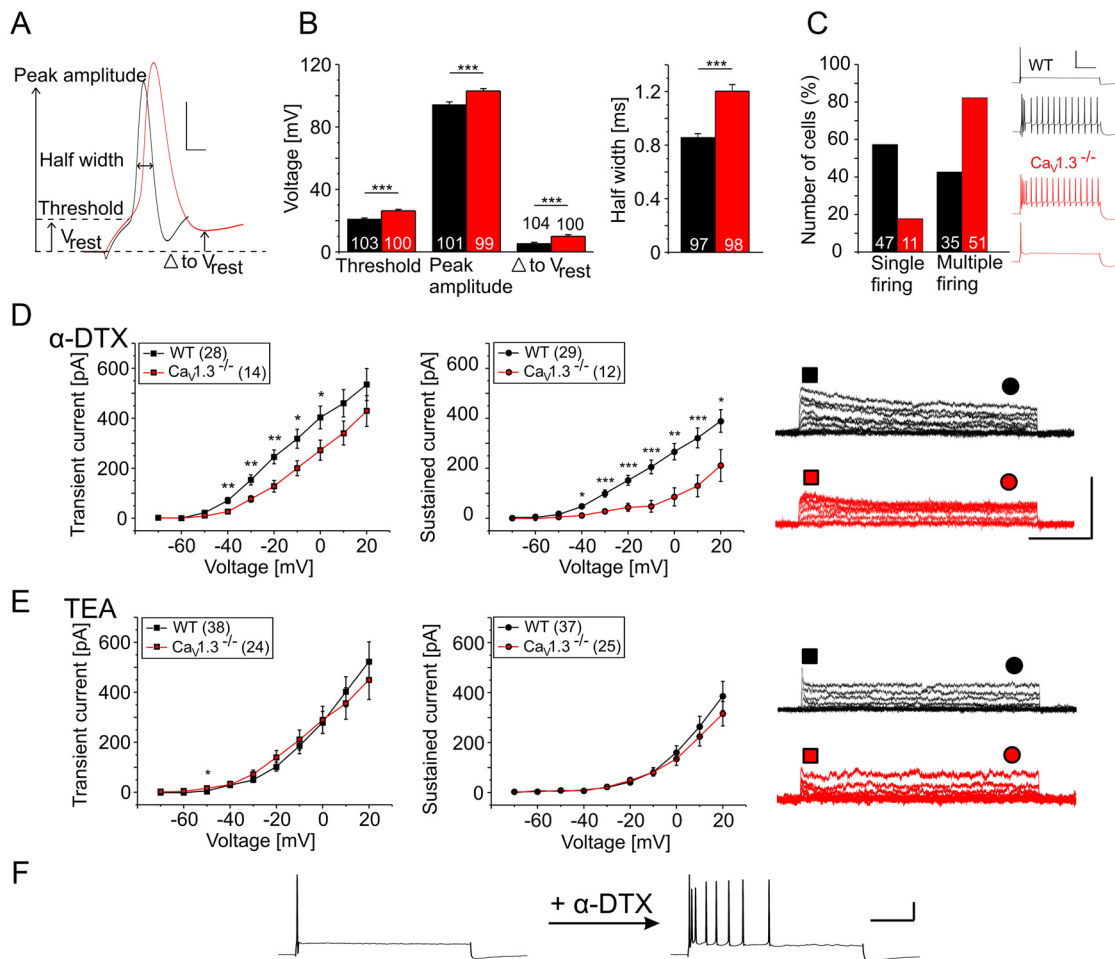
Figure 8. Changes in AP properties, current–voltage relations, and potassium currents in Ca$_v$1.3$^{-/-}$ LSO neurons. **A**, First AP of a WT and a Ca$_v$1.3$^{-/-}$ P12 LSO neuron (black and red trace, respectively; also in **C**, **E**, **F**) in response to a rectangular current injection (+450 pA for 200 ms), illustrating the parameters analyzed in **B**. Calibration: 30 mV, 1 ms. **B**, Compared with the WT, APs of Ca$_v$1.3$^{-/-}$ neurons displayed a higher threshold, a higher peak amplitude, a greater difference between the maximal repolarization and V_{rest}, and a longer half width. **C**, Upon rectangular current injection (+450 pA for 200 ms), the great majority of Ca$_v$1.3$^{-/-}$ neurons (51 of 62, 82%) responded with a multiple AP firing pattern, whereas the rest displayed only a single AP. In contrast, only a minority of WT neurons (35 of 82, 43%) displayed multiple APs. Inset shows examples of single and multiple firing neurons in both WT and Ca$_v$1.3$^{-/-}$ mice. Calibration: 40 mV, 50 ms. **D**, α-DTX-sensitive potassium currents were smaller in Ca$_v$1.3$^{-/-}$ LSO neurons. Results for the transient and the sustained component are depicted in the left and right panel, respectively, and representative traces of α-DTX-sensitive currents are shown on the right. Calibration: 1 nA, 100 ms. **E**, TEA-sensitive currents displayed virtually no differences between genotypes. Layout and calibration as in **D**. **F**, Exemplary voltage recordings of a WT neuron whose firing behavior was converted from a single to a multiple type upon application of α-DTX. Calibration: 20 mV, 50 ms. Numbers in bars (**B**, **C**) and in brackets (**D**, **E**) depict numbers of analyzed neurons. *$p < 0.05$; **$p < 0.01$; ***$p < 0.001$.

ponent of excitatory transmission declines drastically with age in the auditory brainstem (Bellingham et al., 1998; Taschenberger and von Gersdorff, 2000; Youssoufian et al., 2005; Lu and Trussell, 2007). For example, in the mouse MNTB, NMDA EPSCs increase until P11/12, after which they decline to very low or undetectable levels at P16 (Joshi and Wang, 2002). We thus addressed the question of whether such a scenario is also present in LSO neurons and whether it is affected in Ca$_v$1.3$^{-/-}$ LSO neurons. To isolate and analyze NMDA EPSCs, the recorded LSO neurons were clamped to +40 mV, a voltage at which the voltage-dependent Mg^{2+} block of the NMDA receptors is removed (Kampa et al., 2004). From the resulting responses, which comprised nonNMDA as well as NMDA EPSCs, the nonNMDA components were digitally subtracted (Fig. 11A). In WT neurons, the peak amplitude of the NMDA EPSCs displayed a postnatal developmental decrease (91% between P3 and P19), similar to the observations made in other brain regions. In contrast, the peak amplitude of Ca$_v$1.3$^{-/-}$ LSO neurons did not change significantly between P3 and P12. However, a significant decrease was

observed from P12 to P19 (87%). No differences were found between genotypes of the same age (Table 4, Fig. 11B,C).

The decay time constant of NMDA EPSCs decreased with age in both WT mice and Ca$_v$1.3$^{-/-}$ mice. At P12, NMDA EPSCs lasted longer in Ca$_v$1.3$^{-/-}$, but there were no differences at P3 and P19 (Table 4, Fig. 11D,E). As the decay time of NMDA EPSCs is determined by the subtype composition of the receptors, with NR2A and NR2B subunits leading to long and short time constants, respectively (Dingledine et al., 1999; Cull-Candy et al., 2001), our results allow to conclude that the NR2A-NR2B exchange takes place in a delayed manner in Ca$_v$1.3$^{-/-}$ mice. Finally, the ratio of the NMDA EPSC peak amplitudes to the nonNMDA EPSC peak amplitudes was calculated. It decreased with age in both WT and Ca$_v$1.3$^{-/-}$ mice. At P12, the ratio was higher in Ca$_v$1.3$^{-/-}$ mice, with no differences at P3 and P19 (Table 4, Fig. 11F,G). In summary, in contrast to the nonNMDA component, the development of the NMDA component of excitatory inputs to the LSO was retarded in Ca$_v$1.3$^{-/-}$ mice. Nevertheless, at P19, none of the three parameters tested was different any more.
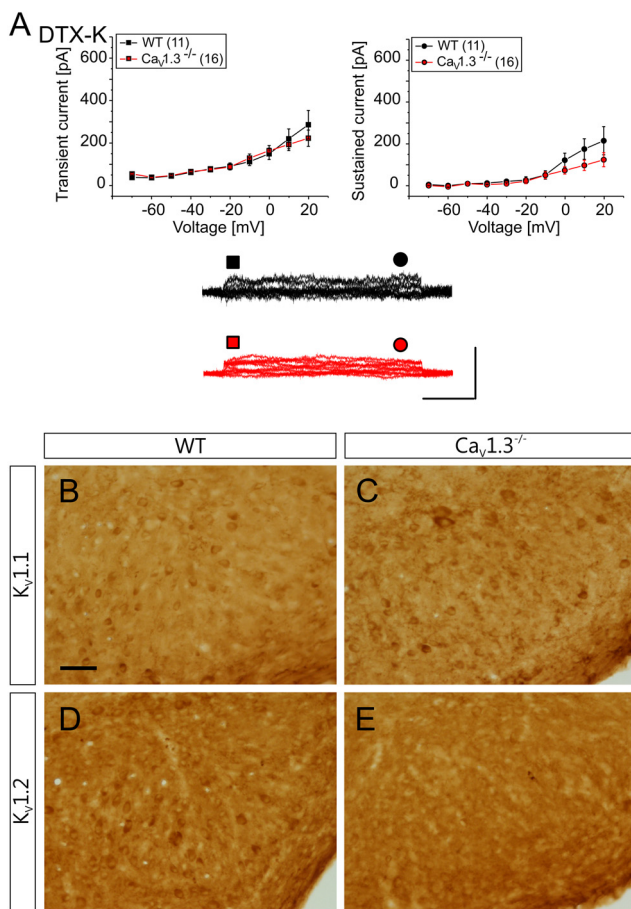
Figure 9. Analysis of $K_v1.1$ and $K_v1.2$ subunits in WT and $Ca_v1.3^{-/-}$ LSO neurons. **A**, P12 LSO neurons displayed DTX-K-sensitive currents that showed no differences between genotypes in the transient and the sustained components. Calibration: 1 nA, 100 ms. Numbers in brackets depict numbers of analyzed neurons. **B**, **C**, Immunohistochemistry against the $K_v1.1$ subunit. $K_v1.1$ immunoreactivity was detected in both WT and $Ca_v1.3^{-/-}$ mice. **D**, **E**, Immunohistochemistry against the $K_v1.2$ subunit. Whereas LSO neurons of WT mice were immunopositive for Kv1.2, those in $Ca_v1.3^{-/-}$ mice were virtually unlabeled. Scale bar: (in **B**) **B**–**E**, 50 μm. Dorsal is up, lateral is to the right.

LSO neurons possess functional $Ca_v1.3$ channels

In a last series of experiments, we addressed the question whether functional calcium channels containing the $Ca_v1.3$ subunit are present in the LSO neurons themselves. An answer to this question is important because it would contribute to the identification of possible causes of the developmental malformation and neuron loss in the $Ca_v1.3^{-/-}$ LSO. We performed Ca^{2+} imaging of single LSO neurons in slices of P3 animals of both genotypes to assess differences in L-type Ca^{2+} channel-mediated currents. Depolarization by high K^+ lead to a Ca^{2+} influx in both WT and $Ca_v1.3^{-/-}$ mice (Fig. 12A,B). In the presence of the L-type Ca^{2+} channel blocker nifedipine, the response decreased in both genotypes, yet the nifedipine-sensitive component was significantly smaller in $Ca_v1.3^{-/-}$ ($32 \pm 2.3\%$) compared with WT ($42 \pm 1.5\%$; $p = 0.0002$) (Fig. 11D). This difference can be assigned to the missing of the $Ca_v1.3$, showing its presence in WT LSO cells.

Discussion

Our study demonstrates three important findings upon loss of the pore-forming α_{1D} subunit of $Ca_v1.3$ calcium channels. First, the LSO, a key nucleus in the auditory brainstem, is strikingly malformed, its volume is drastically reduced (by 58%), and its
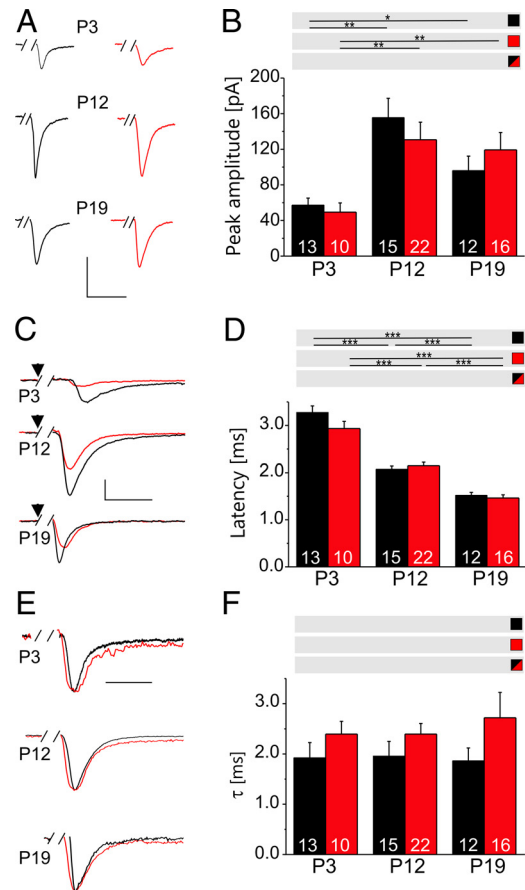

Figure 10. Normal development of the nonNMDA component of excitatory inputs into the LSO of $Ca_v1.3^{-/-}$ mice. **A**, Examples of nonNMDA EPSCs in LSO neurons, illustrating the age dependency of their amplitude. EPSCs were evoked by stimulation of the CN afferents in slices of WT and $Ca_v1.3^{-/-}$ animals (also in **C**, **E**). Calibration: 100 pA, 5 ms; stimulus artifacts were removed from these and all following recordings. **B**, The peak amplitude of the nonNMDA EPSCs increased from P3 to P12 in both WT and $Ca_v1.3^{-/-}$ mice. No further increase occurred between P12 and P19 in both groups. Notably, there was no difference between WT and $Ca_v1.3^{-/-}$ mice at all three age comparisons. **C**, Examples of nonNMDA EPSCs in LSO neurons, illustrating the age dependency of their onset latency. Calibration: 50 pA, 5 ms; arrowheads mark beginning of stimuli. **D**, The latency of the EPSCs decreased between P3 and P19 in both WT and $Ca_v1.3^{-/-}$ mice. As with peak amplitude, there was no difference in latency between WT and $Ca_v1.3^{-/-}$ mice at all three age comparisons. $*p < 0.05$; $**p < 0.01$; $***p < 0.001$. **E**, Examples of scaled nonNMDA EPSCs in LSO neurons, illustrating the age independency of their duration. Calibration, 5 ms. **F**, The decay time constant τ did not change between both P3–P12 and P12–P19. Likewise, there were no differences between WT and $Ca_v1.3^{-/-}$. Numbers in bars depict number of analyzed neurons. Gray horizontal bars depict statistical information regarding the WT group, the $Ca_v1.3^{-/-}$ groups, and the WT vs $Ca_v1.3^{-/-}$ group (black, red, and black/red, respectively).

neuron number is greatly decreased (by 33%). Second, a volume reduction occurs in all auditory brainstem regions, albeit generally to a lesser degree than in the LSO. Third, the 1100 neurons that remain in the $Ca_v1.3^{-/-}$ LSO display many normal features, both in terms of morphology and physiology. Moreover, two essential physiological features are strikingly altered in $Ca_v1.3^{-/-}$ LSO neurons, namely the AP kinetics and the predominantly multiple AP firing pattern in response to current injection, whereas a single firing pattern predominates in WTs. The latter findings can be explained by a reduction of LTK conductances. The data show that the LSO comprises two populations of neurons: those (1/3) that are very vulnerable to missing $Ca_v1.3$ channel activity during early development and those (2/3) that are rather resistant and, to a large extent, display normal features,

Table 4. Excitatory synaptic inputs of the LSO

	P3			P12			P19		
	WT	Ca$_v$1.3$^{-/-}$	p value	WT	Ca$_v$1.3$^{-/-}$	p value	WT	Ca$_v$1.3$^{-/-}$	p value
NonNMDA									
Peak amplitude [pA]	57.2 ± 8	49.4 ± 10.4	0.55	155.4 ± 21.1	130.7 ± 23	0.49	96 ± 16.3	119.4 ± 19.5	0.39
t test WT			0.0007[a]			0.057[b]			0.049[c]
Ca$_v$1.3$^{-/-}$			0.003[a]			0.72[b]			0.004[c]
Onset latency [ms]	3.28 ± 0.14	2.93 ± 0.15	0.11	2.09 ± 0.07	2.15 ± 0.07	0.52	1.58 ± 0.11	1.46 ± 0.07	0.34
t test WT			2.3×10^{-8a}			0.0007[b]			2.5×10^{-9c}
Ca$_v$1.3$^{-/-}$			8×10^{-6a}			5.6×10^{-8b}			6.2×10^{-10c}
Tau [ms]	1.93 ± 0.3	2.4 ± 0.26	0.25	1.97 ± 0.28	2.4 ± 0.21	0.22	1.86 ± 0.26	2.72 ± 0.5	0.14
t test WT			0.92[a]			0.79[b]			0.87[c]
Ca$_v$1.3$^{-/-}$			0.99[a]			0.56[b]			0.57[c]
NMDA									
Peak amplitude [pA]	56 ± 12.3	38.6 ± 10.3	0.29	22.6 ± 4.8	63.5 ± 19.2	0.055	5.2 ± 1.2	8.1 ± 1.9	0.22
t test WT			0.024[a]			0.004[b]			0.002[c]
Ca$_v$1.3$^{-/-}$			0.26[a]			0.012[b]			0.016[c]
Tau [ms]	110.9 ± 8.8	133.7 ± 19.1	0.24	35.2 ± 4.1	54.8 ± 4.8	0.0047	19.3 ± 2.5	18.5 ± 3.6	0.87
t test WT			1.4×10^{-6a}			0.028[b]			5.9×10^{-7c}
Ca$_v$1.3$^{-/-}$			0.0013[a]			0.0001[b]			6.9×10^{-5c}
NMDA/nonNMDA	1.14 ± 0.22	0.94 ± 0.21	0.54	0.17 ± 0.03	0.4 ± 0.07	0.006	0.06 ± 0.01	0.09 ± 0.02	0.28
t test WT			0.0016[a]			0.0037[b]			0.0008[c]
Ca$_v$1.3$^{-/-}$			0.036[a]			0.0007[b]			0.0031[c]

Ten to twenty-two neurons in 3–11 slices were analyzed for each parameter.

[a]P3–P12.

[b]P12–P19.

[c]P3–P19.

with the exception of LTK currents and, as a consequence, the spiking behavior.

Possible causes of the impaired development
We observed several structural changes in the auditory brainstem centers upon Ca$_v$1.3 channel loss, with the most striking in the LSO and, interestingly, not observed in other peripheral deafness models. These changes are manifest clearly before hearing onset and may be the result of impaired neurogenesis and/or extensive apoptosis. Two causes may account for the changes. In the first place, the missing cochlea-driven activity, which results from the complete absence of Ca$_v$1-mediated currents in IHCs (Platzer et al., 2000; Brandt et al., 2003), may deprive the auditory brainstem of indispensable synaptic input. The changes would thus be the result of peripheral deafness. However, as the structural defects become manifest long before hearing onset, the peripheral deafness would implicate a lack of input provided by spontaneous activity. Spontaneous activity in IHCs before hearing onset, involving firing of Ca^{2+} APs and exocytosis, is well documented in rats (Glowatzki and Fuchs, 2002; Tritsch et al., 2007; Tritsch and Bergles, 2010) and mice (Kros et al., 1998; Beutner and Moser, 2001). As the IHCs are the primary sensory cells in the cochlea and as functional connectivity within the auditory brainstem is established prenatally (Friauf and Kandler, 1990; Kandler and Friauf, 1993, 1995), the spontaneous activity may be transmitted into subsequent auditory centers. In fact, rhythmic AP activity in immature auditory brainstem regions before hearing onset has been described in several species (Woolf and Ryan, 1985; Walsh and Mcgee, 1987; Gummer and Mark, 1994; Lippe, 1994; Kotak and Sanes, 1995; Moore et al., 1995). Afferent synaptic activity is of uttermost importance for survival and maturation of central auditory neurons (Sanes and Takács, 1993; Koch and Sanes, 1998). Therefore, it is plausible that the structural changes presented in this paper are primarily caused by the missing activity in IHCs and are thus down-stream effects of peripheral defects.

However, in the second place, it is also plausible that the structural changes occur in the Ca$_v$1.3$^{-/-}$ auditory brainstem centers because vitally important Ca^{2+} influx has ceased directly in the neurons within these centers. This scenario would thus reflect on-site effects and represent a form of central hearing disability. Ca^{2+} influx into LSO neurons has been identified via calcium imaging and can be blocked by nifedipine (Kullmann et al., 2002; Kullmann and Kandler, 2008), implying the presence of functional Ca$_v$1 channels in these cells. Survival of LSO neurons in organotypic slice cultures, in which the cells are deprived of peripheral input, requires the activity of Ca$_v$1 channels (Ehrlich et al., 1998; Lohmann et al., 1998). Our Fura2-imaging data obtained in the presence of nifedipine in WT and Ca$_v$1.3$^{-/-}$ LSO neurons point to the presence of functional Ca$_v$1.3 channels. Preliminary electrophysiological data indicate that a given LSO neuron possesses functional Ca$_v$1.3 as well as Ca$_v$1.2 channels (Tarabova et al., 2009). Therefore, on-site loss of calcium channels in Ca$_v$1.3$^{-/-}$ LSO neurons themselves may be the central cause of the impaired development described here, rather than the peripheral defects. The two mechanisms are not mutually exclusive and may act together. At present, it remains open to what extent the absence of peripheral or central Ca$_v$1.3 channels contributes to the developmental impairments. This awaits differential analysis of mice with tissue-specific Ca$_v$1.3 deletion either in the cochlea or the brainstem. We hypothesize that the central loss has a considerable, although not exclusive impact, because other deafness-related gene mutations, which cause function loss in the cochlea, e.g., in *dn/dn* mice (Youssoufian et al., 2008), otoferlin *otof* mice (Longo-Guess et al., 2007), and prosaposin$^{-/-}$ mice (Akil et al., 2006), appear not to result in obvious LSO malformations.

Ca$_v$1.3 and potassium channels
Our electrophysiological investigations encompassed those LSO neurons that remained in Ca$_v$1.3$^{-/-}$ mice. Out of a total of 16
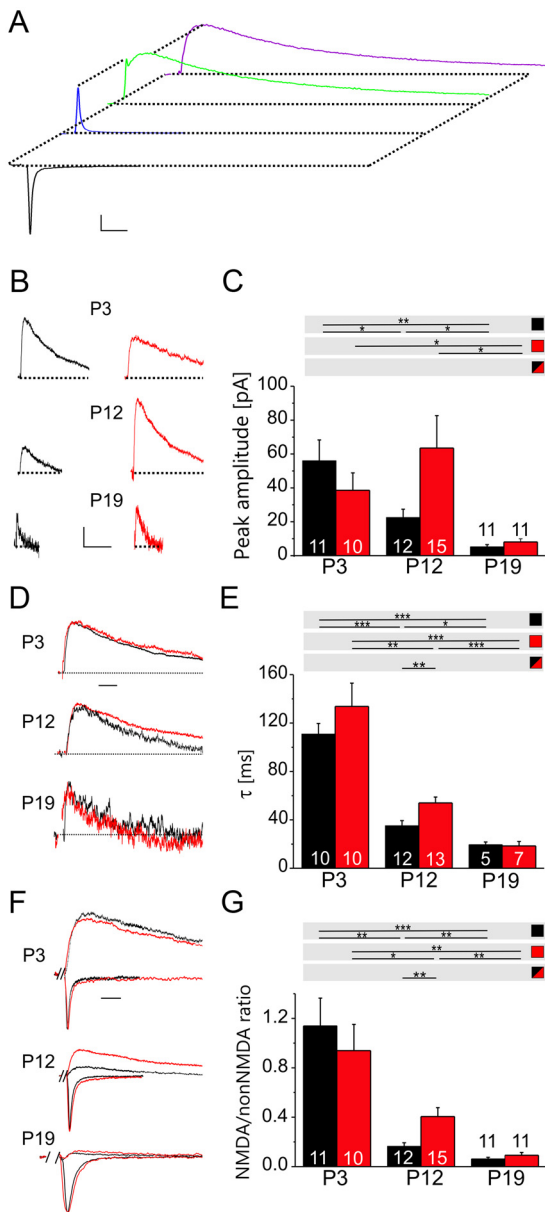
Figure 11. Delayed development of the NMDA component of excitatory inputs into the LSO of Ca$_v$1.3$^{-/-}$ mice. **A**, The NMDA EPSCs were isolated as follows: recordings obtained at $V_H = -70$ mV (black trace) were inverted and scaled (blue trace) to the first peak amplitude of the recordings obtained at $V_H = +40$ mV (green trace); digital subtraction of the blue trace from the green one resulted in the NMDA component (purple trace). Calibration: 100 pA, 10 ms. **B**, Examples of NMDA EPSCs in LSO neurons, illustrating the age dependency of their amplitude in WT (black) and Ca$_v$1.3$^{-/-}$ (red) animals. Calibrations: P3 and P12, 20 pA and 50 ms; P19, 5 pA and 50 ms. **C**, The peak amplitude of the NMDA EPSCs decreased with age in WT mice, both between P3–P12 and P12–P19. In contrast, there was no decrease from P3 to P12 in Ca$_v$1.3$^{-/-}$ mice, yet a drastic decrease from P12 to P19. There was no difference between phenotypes at each age. **D**, Examples of scaled NMDA EPSCs, illustrating the age dependency of their duration. Calibration, 10 ms. **E**, The decay time constant τ decreased with age in both phenotypes. At P12, EPSCs lasted longer in Ca$_v$1.3$^{-/-}$ animals. In some cases, NMDA responses were too small to analyze the decay time, explaining the lower numbers compared with **C** and **G**. **F**, Examples of nonNMDA and NMDA EPSCs, illustrating the ratio of the two components. For each age, two neurons are depicted (one WT and one Ca$_v$1.3$^{-/-}$), whose responses were scaled such that the nonNMDA EPSCs had the same peak amplitude and the NMDA traces were aligned accordingly. Calibration, 10 ms. **G**, The NMDA/nonNMDA peak amplitude ratio decreased with age in both genotypes. Notably, the ratio was higher in P12 Ca$_v$1.3$^{-/-}$ mice than in WT animals. See legend for Figure 10 for further information. *$p < 0.05$; **$p < 0.01$; ***$p < 0.001$.
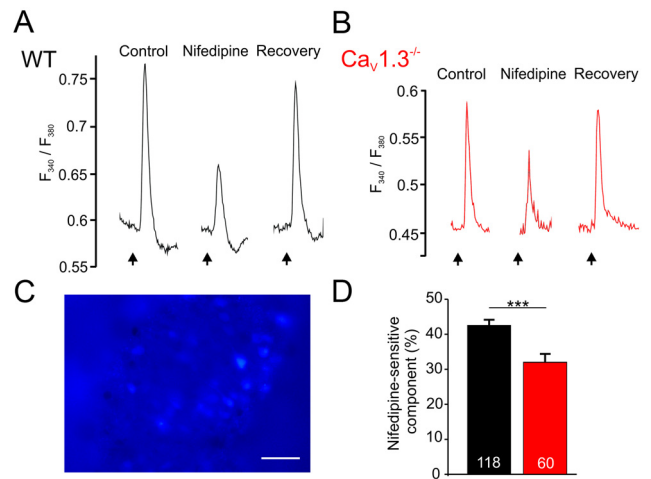

Figure 12. Functional Ca$_v$1.3 channels mediate calcium influx in LSO neurons. **A**, **B**, Examples of Fura2 fluorescence changes in a single WT and a single Ca$_v$1.3$^{-/-}$ LSO neuron in response to depolarization by 30 mM K$^+$ in the bath solution. Ca^{2+} responses decreased in the presence of nifedipine (20 μM) and recovered after washout. Arrows mark the beginning of the 15-s-long K$^+$ application pulse. **C**, Fura2-stained LSO cells from a P3 WT mouse, shown in false colors. Analyzed cells are marked. Scale bar, 100 μm. **D**, The nifedipine-sensitive component of the Fura2 signal was significantly smaller in Ca$_v$1.3$^{-/-}$ than in WT. Numbers in bars depict number of analyzed neurons. ***$p < 0.001$.

biophysical and synaptic properties analyzed, seven differed between the two phenotypes. The major difference occurred in the reduction of α-DTX-sensitive LTK currents, presumably being mediated through K$_v$1.2 channels. Considering that such currents sculpture several of the changed biophysical properties, many of our observed changes likely reflect secondary effects. Our results thus indicate that the remaining 2/3 of LSO neurons may be quite invulnerable to the Ca$_v$1.3 loss. Indeed, the glutamatergic inputs develop normally but are retarded. Likewise, functional inhibitory glycinergic inputs are present in the knockouts (Hirtz and Friauf, unpublished observations). Therefore, Ca$_v$1.3$^{-/-}$ LSO neurons appear to be structurally and functionally integrated into the brainstem circuitry. However, currents through α-DTX-sensitive potassium channels contribute to short EPSPs and high reliability and temporal fidelity of synaptic transmission (Brew and Forsythe, 1995; Kaczmarek et al., 2005). They also determine the rate and timing of APs (Dodson et al., 2002) and thus preserve (and possibly enhance) phase-locking behavior. Therefore, the reduction of the α-DTX-sensitive currents in Ca$_v$1.3$^{-/-}$ LSO neurons and the subsequent secondary effects are likely to make these cells unable to properly integrate synaptic signals. Inevitably, this will result in a functional impairment in the auditory brainstem and will, therefore, represent a form of central auditory processing disorders. Interestingly, LSO neurons of P13–P16 *dn/dn* mice display a mainly single firing behavior, whereas in WT, the ratio of single and multiple responders is approximately equal (Couchman et al., 2011). As this contrasts with the multiple firing pattern in Ca$_v$1.3$^{-/-}$ mice, it further supports the idea of an on-site role of Ca$_v$1.3 during auditory brainstem development.

The finding of altered firing behavior and a reduction of α-DTX-sensitive currents in Ca$_v$1.3$^{-/-}$ LSO neurons is consistent with a role of Ca$_v$1.3 channels in the activity-dependent transcriptional regulation of potassium channels. Indeed, Ca$_v$1.3 loss results in reduced BK$_{Ca}$ conductances in cochlear hair cells (Nemzou et al., 2006) and chromaffin cells (Marcantoni et al., 2010), further supporting the idea that Ca$_v$1.3 channel activity

leads to changes in gene expression and ultimately to long-term alterations in neuronal function. Nevertheless, there may also be a direct contribution of $Ca_v1.3$-mediated currents to the initiation of APs, as $Ca_v1.3$ channels open at subthreshold depolarizations that do not activate $Ca_v1.2$ channels (Lipscombe et al., 2004). This may also explain the higher AP threshold in our $Ca_v1.3^{-/-}$ LSO neurons and is consistent with a main contribution of $Ca_v1.3$ to the early phase of depolarization. Indeed, LSO neurons express a sufficient amount of functional $Ca_v1.3$ channels, as evidenced by our Fura2 measurements. A direct role of $Ca_v1.3$ in the generation of spontaneous AP activity has been demonstrated in the substantia nigra (Chan et al., 2007), the sinoatrial node (Zhang et al., 2002), and chromaffin cells (Marcantoni et al., 2010).

Role of Ca_v1 channels in the brain

Within the Ca_v1 family of VGCCs, prominent expression in the brain has been demonstrated for $Ca_v1.2$ and $Ca_v1.3$, while only very low levels were found for $Ca_v1.1$ and $Ca_v1.4$ (Sukiasyan et al., 2009; Sinnegger-Brauns et al., 2009). In contrast to the plethora of data accumulated from adult mice (for review, see, Striessnig et al., 2006; Striessnig and Koschak, 2008), very little is known about a crucial role of $Ca_v1.3$ or $Ca_v1.2$ in brain development. A C-terminal fragment of $Ca_v1.2$ (CCAT) translocates to the nucleus and directly activates transcription; nuclear CCAT is low in the perinatal cortex and increases with age, whereas membrane-bound $Ca_v1.2$ channel immunoreactivity peaks at P8 and has declined by P21 (Gomez-Ospina et al., 2006). Both findings imply a developmental role of $Ca_v1.2$. By demonstrating the crucial requirement of $Ca_v1.3$ in circuit formation in the central auditory system, the present study adds a new facet to the developmental roles of Ca_v1 channels in the brain and a new variant to the growing list of Ca_v1-related channelopathies (Liao and Soong, 2010; Striessnig et al., 2010).

Conclusions

Our findings imply a requirement of $Ca_v1.3$ channels during brainstem development, which is of particular importance in the auditory system. A malformation of the LSO has not been described in other deafness models that lack spontaneous activity of cochlear origin. We argue that two factors contribute synergistically to the unique $Ca_v1.3^{-/-}$ LSO phenotype, namely on-site loss of $Ca_v1.3$ channels in LSO neurons plus the lack of peripheral input. In line with this, we conclude that input from the cochlea and Ca^{2+} influx via $Ca_v1.3$ channels are indispensable for normal LSO development. The relative importance of the two factors is elusive at present. Conditional knock-out mice in which the $Ca_v1.3$ gene is deleted either in the cochlea or in the brainstem will help to clarify this question. In humans, mutations of the $Ca_v1.2$ gene result in a gain of function (through a nearly complete loss of VGCC inactivation) and multisystem disorders (Splawski et al., 2004). $Ca_v1.3$ gene mutations in humans have very recently been reported (Baig et al., 2011); as expected from the mouse model, they result in deafness and sinoatrial node malfunction. Based on our study, they should also affect circuit development in the auditory brainstem.

References

Akil O, Chang J, Hiel H, Kong JH, Yi E, Glowatzki E, Lustig LR (2006) Progressive deafness and altered cochlear innervation in knock-out mice lacking prosaposin. J Neurosci 26:13076–13088.

Alford BR, Ruben RJ (1963) Physiological, behavioral and anatomical correlates of the development of hearing in the mouse. Ann Otol Rhinol Laryngol 72:237–247.

Baig SM, Koschak A, Lieb A, Gebhart M, Dafinger C, Nürnberg G, Ali A, Ahmad I, Sinnegger-Brauns MJ, Brandt N, Engel J, Mangoni ME, Farooq M, Khan HU, Nürnberg P, Striessnig J, Bolz HJ (2011) Loss of Ca(v)1.3 (CACNA1D) function in a human channelopathy with bradycardia and congenital deafness. Nat Neurosci 14:77–84.

Barnes-Davies M, Barker MC, Osmani F, Forsythe ID (2004) Kv1 currents mediate a gradient of principal neuron excitability across the tonotopic axis in the rat lateral superior olive. Eur J Neurosci 19:325–333.

Bellingham MC, Lim R, Walmsley B (1998) Developmental changes in EPSC quantal size and quantal content at a central glutamatergic synapse in rat. J Physiol 511:861–869.

Beutner D, Moser T (2001) The presynaptic function of mouse cochlear inner hair cells during development of hearing. J Neurosci 21:4593–4599.

Blaesse P, Ehrhardt S, Friauf E, Nothwang HG (2005) Developmental pattern of three vesicular glutamate transporters in the rat superior olivary complex. Cell Tissue Res 320:33–50.

Boudreau JC, Tsuchitani C (1970) Cat superior olive s-segment cell discharge to tonal stimulation. In: Contributions to sensory physiology (Neff WD, ed), pp 143–213. New York: Academic.

Brandt A, Striessnig J, Moser T (2003) $Ca_v1.3$ channels are essential for development and presynaptic activity of cochlear inner hair cells. J Neurosci 23:10832–10840.

Brew HM, Forsythe ID (1995) Two voltage-dependent K^+ conductances with complementary functions in postsynaptic integration at a central auditory synapse. J Neurosci 15:8011–8022.

Caird D, Klinke R (1983) Processing of binaural stimuli by cat superior olivary complex neurons. Exp Brain Res 52:385–399.

Cang J, Rentería RC, Kaneko M, Liu X, Copenhagen DR, Stryker MP (2005) Development of precise maps in visual cortex requires patterned spontaneous activity in the retina. Neuron 48:797–809.

Catterall WA, Perez-Reyes E, Snutch TP, Striessnig J (2005) International union of pharmacology. XLVIII. Nomenclature and structure-function relationships of voltage-gated calcium channels. Pharmacol Rev 57:411–425.

Chan CS, Guzman JN, Ilijic E, Mercer JN, Rick C, Tkatch T, Meredith GE, Surmeier DJ (2007) 'Rejuvenation' protects neurons in mouse models of Parkinson's disease. Nature 447:1081–1086.

Clark NC, Nagano N, Kuenzi FM, Jarolimek W, Huber I, Walter D, Wietzorrek G, Boyce S, Kullmann DM, Striessnig J, Seabrook GR (2003) Neurological phenotype and synaptic function in mice lacking the $Ca_v1.3$ α subunit of neuronal L-type voltage-dependent Ca^{2+} channels. Neuroscience 120:435–442.

Coetzee WA, Amarillo Y, Chiu J, Chow A, Lau D, McCormack T, Moreno H, Nadal MS, Ozaita A, Pountney D, Saganich M, Vega-Saenz de Miera E, Rudy B (1999) Molecular diversity of K^+ channels. Ann N Y Acad Sci 868:233–285.

Couchman K, Garrett A, Deardorff AS, Rattay F, Resatz S, Fyffe R, Walmsley B, Leao RN (2011) Lateral superior olive function in congenital deafness. Hear Res. Advance online publication. Retrieved May 19, 2011. doi:10.1016/heares.2011.01.012.

Crair MC, Malenka RC (1995) A critical period for long-term potentiation at thalamocortical synapses. Nature 375:325–328.

Cull-Candy S, Brickley S, Farrant M (2001) NMDA receptor subunits: diversity, development and disease. Curr Opin Neurobiol 11:327–335.

Dallwig R, Vitten H, Deitmer JW (2000) A novel barium-sensitive calcium influx into rat astrocytes at low external potassium. Cell Calcium 28:247–259.

Dingledine R, Borges K, Bowie D, Traynelis SF (1999) The glutamate receptor ion channels. Pharmacol Rev 51:7–61.

Dodson PD, Barker MC, Forsythe ID (2002) Two heteromeric K_v1 potassium channels differentially regulate action potential firing. J Neurosci 22:6953–6961.

Ehret G (1976) Development of absolute auditory thresholds in the house mouse. J Am Audiol Soc 1:179–184.

Ehrlich I, Ilic V, Lohmann C, Friauf E (1998) Development of glycinergic transmission in organotypic cultures from auditory brain stem. Neuroreport 9:2785–2790.

Erazo-Fischer E, Striessnig J, Taschenberger H (2007) The role of physiological afferent nerve activity during in vivo maturation of the calyx of Held synapse. J Neurosci 27:1725–1737.

Friauf E (1993) Transient appearance of calbindin-D_{28k}-positive neurons in

the superior olivary complex of developing rats. J Comp Neurol 334: 59–74.

Friauf E, Kandler K (1990) Auditory projections to the inferior colliculus of the rat are present by birth. Neurosci Lett 120:58–61.

Friauf E, Lohmann C (1999) Development of auditory brainstem circuitry: activity-dependent and activity-independent processes. Cell Tissue Res 297:187–195.

Friauf E, Aragón C, Löhrke S, Westenfelder B, Zafra F (1999) Developmental expression of the glycine transporter GLYT2 in the auditory system of rats suggests involvement in synapse maturation. J Comp Neurol 412:17–37.

Gittelman JX, Tempel BL (2006) Kv1.1-containing channels are critical for temporal precision during spike initiation. J Neurophysiol 96:1203–1214.

Glowatzki E, Fuchs PA (2002) Transmitter release at the hair cell ribbon synapse. Nat Neurosci 5:147–154.

Glueckert R, Wietzorrek G, Kammen-Jolly K, Scholtz A, Stephan K, Striessnig J, Schrott-Fischer A (2003) Role of class D L-type Ca^{2+} channels for cochlear morphology. Hear Res 178:95–105.

Gomez-Ospina N, Tsuruta F, Barreto-Chang O, Hu L, Dolmetsch R (2006) The C terminus of the L-type voltage-gated calcium channel Cav1.2 encodes a transcription factor. Cell 127:591–606.

Grigg JJ, Brew HM, Tempel BL (2000) Differential expression of voltage-grated potassium channel genes in auditory nuclei of the mouse brainstem. Hear Res 140:77–90.

Grothe B, Pecka M, McAlpine D (2010) Mechanisms of sound localization in mammals. Physiol Rev 90:983–1012.

Gummer AW, Mark RF (1994) Patterned neural activity in brain stem auditory areas of a prehearing mammal, the tammar wallaby (*Macropus eugenii*). Neuroreport 5:685–688.

Guzman JN, Sánchez-Padilla J, Chan CS, Surmeier DJ (2009) Robust pacemaking in substantia nigra dopaminergic neurons. J Neurosci 29:11011–11019.

Hack MA (1968) The developmental Preyer reflex in the sh-1 mouse. J Aud Res 8:449–457.

Hell JW, Westenbroek RE, Warner C, Ahlijanian MK, Prystay W, Gilbert MM, Snutch TP, Catterall WA (1993) Identification and differential subcellular localization of the neuronal class C and class D L-type calcium channel a1 subunits. J Cell Biol 123:949–962.

Hsia AY, Malenka RC, Nicoll RA (1998) Development of excitatory circuitry in the hippocampus. J Neurophysiol 79:2013–2024.

Huberman AD, Feller MB, Chapman B (2008) Mechanisms underlying development of visual maps and receptive fields. Annu Rev Neurosci 31:479–509.

Joshi I, Wang LY (2002) Developmental profiles of glutamate receptors and synaptic transmission at a single synapse in the mouse auditory brainstem. J Physiol 540:861–873.

Kaczmarek LK, Bhattacharjee A, Desai R, Gan L, Song P, von Hehn CA, Whim MD, Yang B (2005) Regulation of the timing of MNTB neurons by short-term and long-term modulation of potassium channels. Hear Res 206:133–145.

Kampa BM, Clements J, Jonas P, Stuart GJ (2004) Kinetics of Mg^{2+} unblock of NMDA receptors: implications for spike-timing dependent synaptic plasticity. J Physiol 556:337–345.

Kandler K, Friauf E (1993) Pre- and postnatal development of efferent connections of the cochlear nucleus in the rat. J Comp Neurol 328:161–184.

Kandler K, Friauf E (1995) Development of glycinergic and glutamatergic synaptic transmission in the auditory brainstem of perinatal rats. J Neurosci 15:6890–6904.

Kandler K, Gillespie DC (2005) Developmental refinement of inhibitory sound-localization circuits. Trends Neurosci 28:290–296.

Kandler K, Clause A, Noh J (2009) Tonotopic reorganization of developing auditory brainstem circuits. Nat Neurosci 12:711–717.

Karcz A, Hennig MH, Robbins CA, Tempel BL, Rübsamen R, Kopp-Scheinpflug C (2011) Low-voltage activated Kv1.1 subunits are crucial for the processing of sound source location in the lateral superior olive in mice. J Physiol 589:1143–1157.

Khazipov R, Luhmann HJ (2006) Early patterns of electrical activity in the developing cerebral cortex of humans and rodents. Trends Neurosci 29:414–418.

Khazipov R, Esclapez M, Caillard O, Bernard C, Khalilov I, Tyzio R, Hirsch J, Dzhala V, Berger B, Ben-Ari Y (2001) Early development of neuronal activity in the primate hippocampus in utero. J Neurosci 21:9770–9781.

Khazipov R, Sirota A, Leinekugel X, Holmes GL, Ben-Ari Y, Buzsáki G (2004) Early motor activity drives spindle bursts in the developing somatosensory cortex. Nature 432:758–761.

Koch U, Sanes DH (1998) Afferent regulation of glycine receptor distribution in the gerbil LSO. Microsc Res Tech 41:263–269.

Kotak VC, Sanes DH (1995) Synaptically evoked prolonged depolarizations in the developing auditory system. J Neurophysiol 74:1611–1620.

Kros CJ, Ruppersberg JP, Rüsch A (1998) Expression of a potassium current in inner hair cells during development of hearing in mice. Nature 394:281–284.

Kullmann PH, Kandler K (2008) Dendritic Ca^{2+} responses in neonatal lateral superior olive neurons elicited by glycinergic/GABAergic synapses and action potentials. Neuroscience 154:338–345.

Kullmann PH, Ene FA, Kandler K (2002) Glycinergic and GABAergic calcium responses in the developing lateral superior olive. Eur J Neurosci 15:1093–1104.

Leitch B, Szostek A, Lin R, Shevtsova O (2009) Subcellular distribution of L-type calcium channel subtypes in rat hippocampal neurons. Neuroscience 164:641–657.

Liao P, Soong TW (2010) Cav1.2 channelopathies: from arrythmias to autism, bipolar disorder, and immunodeficiency. Pflugers Arch 460:353–359.

Lima PA, Marrion NV (2007) Mechanisms underlying activation of slow AHP in rat hippocampal neurons. Brain Res 1150:74–82.

Lippe WR (1994) Rhythmic spontaneous activity in the developing avian auditory system. J Neurosci 14:1486–1495.

Lipscombe D, Helton TD, Xu W (2004) L-Type calcium channels: The low down. J Neurophysiol 92:2633–2641.

Lohmann C, Ilic V, Friauf E (1998) Development of a topographically organized auditory network in slice culture is calcium dependent. J Neurobiol 34:97–112.

Longo-Guess C, Gagnon LH, Bergstrom DE, Johnson KR (2007) A missense mutation in the conserved C2B domain of otoferlin causes deafness in a new mouse model of DFNB9. Hear Res 234:21–28.

Lu HC, Gonzalez E, Crair MC (2001) Barrel cortex critical period plasticity is independent of changes in NMDA receptor subunit composition. Neuron 32:619–634.

Lu T, Trussell LO (2007) Development and elimination of endbulb synapses in the chick cochlear nucleus. J Neurosci 27:808–817.

Marcantoni A, Vandael DH, Mahapatra S, Carabelli V, Sinnegger-Brauns MJ, Striessnig J, Carbone E (2010) Loss of Cav1.3 channels reveals the critical role of L-Type and BK channel coupling in pacemaking mouse adrenal chromaffin cells. J Neurosci 30:491–504.

Michna M, Knirsch M, Hoda JC, Muenkner S, Langer P, Platzer J, Striessnig J, Engel J (2003) Ca$_v$1.3 (α1D) Ca^{2+} currents in neonatal outer hair cells of mice. J Physiol 15:747–758.

Mikaelian D, Ruben RJ (1965) Development of hearing in the normal CBA-J mouse. Acta Oto-Laryngol 59:451–461.

Moore JK, Perazzo LM, Braun A (1995) Time course of axonal myelination in the human brainstem auditory pathway. Hear Res 87:21–31.

Nemzou NRM, Bulankina AV, Khimich D, Giese A, Moser T (2006) Synaptic organization in cochlear inner hair cells deficient for the Ca(V)1.3 (α1D) subunit of L-type Ca^{2+} channels. Neuroscience 141:1849–1860.

Platzer J, Engel J, Schrott-Fischer A, Stephan K, Bova S, Chen H, Zheng H, Striessnig J (2000) Congenital deafness and sinoatrial node dysfunction in mice lacking class D L-type Ca^{2+} channels. Cell 102:89–97.

Puopolo M, Raviola E, Bean BP (2007) Roles of subthreshold calcium current and sodium current in spontaneous firing of mouse midbrain dopamine neurons. J Neurosci 27:645–656.

Robertson B, Owen D, Stow J, Butler C, Newland C (1996) Novel effects of dendrotoxin homologues on subtypes of mammalian K$_v$1 potassium channels expressed in *Xenopus oocytes*. FEBS Lett 383:26–30.

Rothman JS, Manis PB (2003) Differential expression of three distinct potassium currents in the ventral cochlear nucleus. J Neurophysiol 89:3070–3082.

Sanes DH (1990) An *in vitro* analysis of sound localization mechanisms in the gerbil lateral superior olive. J Neurosci 10:3494–3506.

Sanes DH, Takács C (1993) Activity-dependent refinement of inhibitory connections. Eur J Neurosci 5:570–574.

Shnerson A, Pujol R (1982) Age-related changes in the C57BL/6J mouse cochlea. I. Physiological findings. Dev Brain Res 2:65–75.

Shnerson A, Willott JF (1980) Ontogeny of the acoustic startle response in C57BL/6J mouse pups. J Comp Physiol Psychol 94:36–40.

Sinnegger-Brauns MJ, Huber IG, Koschak A, Wild C, Obermair GJ, Einzinger U, Hoda JC, Sartori SB, Striessnig J (2009) Expression and 1,4-dihydropyridine-binding properties of brain L-type calcium channel isoforms. Mol Pharmacol 75:407–414.

Splawski I, Timothy KW, Sharpe LM, Decher N, Kumar P, Bloise R, Napolitano C, Schwartz PJ, Joseph RM, Condouris K, Tager-Flusberg H, Priori SG, Sanguinetti MC, Keating MT (2004) Ca$_v$1.2 calcium channel dysfunction causes a multisystem disorder including arrhythmia and autism. Cell 119:19–31.

Striessnig J, Koschak A (2008) Exploring the function and pharmacotherapeutic potential of voltage-gated Ca^{2+} channels with gene knockout models. Channels (Austin) 2:233–251.

Striessnig J, Koschak A, Sinnegger-Brauns MJ, Hetzenauer A, Nguyen NK, Busquet P, Pelster G, Singewald N (2006) Role of voltage-gated L-type Ca^{2+} channel isoforms for brain function. Biochem Soc Trans 34:903–909.

Striessnig J, Bolz HJ, Koschak A (2010) Channelopathies in Ca$_v$1.1, Ca$_v$1.3, and Ca$_v$1.4 voltage-gated L-type Ca^{2+} channels. Pflugers Arch 460:361–374.

Sukiasyan N, Hultborn H, Zhang M (2009) Distribution of calcium channel Cav1.3 immunoreactivity in the rat spinal cord and brain stem. Neuroscience 159:217–235.

Tarabova B, Müller B, Friauf E (2009) Voltage-gated calcium channels in the lateral superior olive: wildtype versus knockout mice. Soc Neurosci Abstr 35:36.B/B124.

Taschenberger H, von Gersdorff H (2000) Fine-tuning an auditory synapse for speed and fidelity: developmental changes in presynaptic waveform, EPSC kinetics, and synaptic plasticity. J Neurosci 20:9162–9173.

Tippens AL, Pare JF, Langwieser N, Moosmang S, Milner TA, Smith Y, Lee A (2008) Ultrastructural evidence for pre- and postsynaptic localization of Ca$_v$1.2 L-type Ca^{2+} channels in the rat hippocampus. J Comp Neurol 506:569–583.

Tritsch NX, Bergles DE (2010) Developmental regulation of spontaneous activity in the mammalian cochlea. J Neurosci 30:1539–1550.

Tritsch NX, Yi E, Gale JE, Glowatzki E, Bergles DE (2007) The origin of spontaneous activity in the developing auditory system. Nature 450:50–55.

Tritsch NX, Rodriguez-Conteras A, Crins TTH, Wang HC, Borst JGG, Bergles DE (2010) Calcium action potentials in hair cells pattern auditory neuron activity before hearing onset. Nat Neurosci 13:1–3.

Trussell LO (1999) Synaptic mechanisms for coding timing in auditory neurons. Annu Rev Physiol 61:477–496.

Ulfhake B, Cullheim S (1981) A quantitative light microscopic study of the dendrites of cat spinal gamma-motoneurons after intracellular staining with horseradish peroxidase. J Comp Neurol 202:585–596.

Walsh EJ, Mcgee J (1987) Postnatal development of auditory nerve and cochlear nucleus neuronal responses in kittens. Hear Res 28:97–116.

Wang FC, Bell N, Reid P, Smith LA, McIntosh P, Robertson B, Dolly JO (1999) Identification of residues in dendrotoxin K responsible for its discrimination between neuronal K+ channels containing Kv1.1 and 1.2 alpha subunits. Eur J Biochem 263:222–229.

Webster DB (1985) The spiral ganglion and cochlear nuclei of deafness mice. Hear Res 18:19–27.

Weick JP, Kuo SP, Mermelstein PG (2005) L-type calcium channel regulation of neuronal gene expression. Cellsci Rev 1:44–49.

Woolf NK, Ryan AF (1985) Ontogeny of neural discharge patterns in the ventral cochlear nucleus of the mongolian gerbil. Brain Res 349:131–147.

Youssoufian M, Oleskevich S, Walmsley B (2005) Development of a robust central auditory synapse in congenital deafness. J Neurophysiol 94:3168–3180.

Youssoufian M, Couchman K, Shivdasani MN, Paolini AG, Walmsley B (2008) Maturation of auditory brainstem projections and calyces in the congenitally deaf (dn/dn) mouse. J Comp Neurol 506:442–451.

Zhang Z, Xu Y, Song H, Rodriguez J, Tuteja D, Namkung Y, Shin HS, Chiamvimonvat N (2002) Functional roles of Ca$_v$1.3 (α_{1D}) calcium channel in sinoatrial nodes: insight gained using gene-targeted null mutant mice. Circ Res 90:981–987.